

Ram-pressure stripped radio tails detected in the dynamically active environment of the Shapley Supercluster

P. Merluzzi^{1*}, T. Venturi^{2,3}, G. Busarello¹, G. Di Gennaro^{4,2}, S. Giacintucci⁵, V. Casasola², D. Krajinović⁶, T. Vernstrom⁷, E. Carretti², O. Smirnov^{3,8,2}, K. Trehaven^{7,3,2}, C. S. Anderson⁹, J. Chesters¹⁰, G. Heald¹⁰, A. M. Hopkins¹¹, B. Koribalski^{12,13}

¹ INAF-Osservatorio Astronomico di Capodimonte, salita Moiariello 16, I-80131 Napoli, Italy

² INAF-Istituto di Radioastronomia, via Gobetti 101, I-40129 Bologna, Italy

³ Center for Radio Astronomy Techniques and Technologies, Rhodes University, Grahamstown 6140, South Africa

⁴ Hamburger Sternwarte, Universität Hamburg, Gojenbergsweg 112, 21029 Hamburg, Germany

⁵ Naval research Laboratory, 4555 Overlook Avenue SW, Code 7213, Washington, DC 20375, USA

⁶ Leibniz-Institut für Astrophysik Potsdam (AIP), An der Sternwarte 16, 14482, Potsdam, Germany

⁷ ICRAR, The University of Western Australia, 35 Stirling Hwy, 6009, Crawley, Australia

⁸ South African Radio Astronomy Observatory, 2 Fir Street, Black River Park, Observatory, Cape Town 7925, South Africa

⁹ Research School of Astronomy & Astrophysics, The Australian National University, Canberra ACT 2611, Australia

¹⁰ CSIRO, Space and Astronomy, PO Box 1130, Bentley, WA 6102, Australia

¹¹ School of Mathematical and Physical Sciences, 12 Wally's Walk Macquarie University, NSW 2109, Australia

¹² Australia telescope National Facility, CSIRO Astronomy and Space Science, P.O. Box 76, Epping, NSW 1710, Australia

¹³ School of Science, Western Sydney University, Locked Bag 1797, Penrith, NSW 2751, Australia

Accepted XXX. Received YYY; in original form ZZZ

ABSTRACT

We study the radio continuum emission of four galaxies experiencing ram-pressure stripping in four clusters of the Shapley supercluster at redshift $z \sim 0.05$. Multi-band (235–1367 MHz) radio data, complemented by integral-field spectroscopy, allow us to detect and analyse in detail the non-thermal component both in the galaxy discs and the radio continuum tails. Three galaxies present radio continuum tails which are tens of kiloparsecs long. By deriving the radio spectral index in the inner and outer tails and comparing our findings with the distribution of the extraplanar ionised gas and the results of N -body/hydrodynamical simulations, we demonstrate that these tails are caused by the ram pressure which, together with the ionised gas, sweeps the magnetic field from the galaxy discs. We suggest that the radio continuum emission in these tails can be differently powered by (i) *in situ* star formation; (ii) relativistic electrons stripped from the disc; (iii) shock excitation or a combination of them. All the ram-pressure stripped galaxies are found in environments where cluster-cluster interactions occurred and/or are ongoing thus strongly supporting the thesis that cluster and group collisions and mergers may locally increase the ram pressure and trigger hydrodynamical interactions between the intracluster medium and the interstellar medium of galaxies.

Key words: galaxies: evolution – radio continuum: galaxies – galaxies: ISM – galaxies: clusters: individual: Shapley Supercluster

1 INTRODUCTION

Galaxies orbiting in the cluster environment experience the hydrodynamical interaction of their cold interstellar medium (ISM) with the hot diffuse intracluster medium (ICM). This interplay may result in the ISM evaporation (Cowie & Songalia 1977) and ‘starvation’ (Larson et al. 1980) or may remove the cold gas supply by means of the external pressure exerted by the ICM on the ISM (Gunn & Gott 1972). The primary strength of these processes consists of explaining the lower star formation rates (SFRs; e.g. Balogh et al. 2000) and the redder colours (e.g. Bamford et al. 2009) as well as the HI deficiency (e.g. Guiderdoni & Rocca-Volmerange 1985; Balkowski et al. 2001) seen in cluster galaxies with respect to the field population. At present, galaxy evolution studies support the ram-pressure stripping

(RPS) as the dominant hydrodynamical mechanism contributing to the evolution of cluster galaxies (for a review see Boselli et al. 2022, and references therein).

In their pioneering work Gunn & Gott (1972) modelled the RPS process by means of an analytic expression where the ram pressure opposes the gravitational restoring force per unit area - a decreasing function of the disc radius. It results that in the dense environment of the cluster cores the ram pressure can effectively remove the cooler ISM in the galaxy starting from outside and thus quenching star formation in the ram-pressure stripped regions. Subsequent studies based on observations (e.g. Merluzzi et al. 2016; Brown et al. 2017; Vulcani et al. 2021; Roberts et al. 2021b) and simulations (e.g. Marcolini et al. 2003; Roediger & Hensler 2005; Bekki 2009) showed that the RPS can occur, or start at least, also in less dense environments and/or out of the cluster cores differently

* E-mail: paola.merluzzi@inaf.it

affecting high- and low-mass galaxies. The time-scales for RPS is about one cluster crossing time ($\sim 10^9$ yr).

The characteristic signatures of RPS are the presence of *i*) extraplanar ISM stripped from the galaxy disc in the shape of one-side tail; *ii*) distortion and ultimate truncation of the gaseous disc without corresponding distortion of the old stellar component (Boselli & Gavazzi 2006). Besides, the ISM of late-type galaxies has a multi-phase nature whose components (warm diffuse ionised hydrogen, cold and warm neutral hydrogen, dense molecular gas, interstellar dust), having different surface densities, are differently affected by the ram pressure (see Casasola et al. 2004; Corbelli et al. 2012; Boselli et al. 2014, 2018; Davies et al. 2019; Poggianti et al. 2019; Brown et al. 2021). Moreover, as observed in nearby clusters (e.g. Gavazzi et al. 1995; Miller et al. 2009; Murphy et al. 2009; Vollmer et al. 2004b, 2010, 2013), also the non-thermal component can be stripped from the galaxy discs forming cometary tails. Actually, the first case of late-type galaxies experiencing RPS was detected in the radio continuum (Gavazzi 1978).

It follows that multi-band observations of both the tail and the galaxy are crucial to distinguish among the different components in the tail, and high-resolution observations are required in order to resolve the physics of the gas, the stars and the plasma in the galaxy. Moreover, multi-band studies of individual galaxies affected by RPS are often complemented with dedicated numerical simulations (see Vollmer et al. 2001, 2018; Merluzzi et al. 2013, 2016; Bellhouse et al. 2021)

The effectiveness of such cluster-related mechanism in transforming galaxies encouraged an extensive investigation of RPS supported by the capabilities of the new observing facilities and the availability of focused and highly resolved simulations down to scales of few tens of parsecs. The spectacular appearance of an ongoing RPS also plays a role in the general interest to study the RPS process and contributed to boost systematic searches of RPS candidates, mainly based on visible photometry (Ebeling et al. 2014; McPartland et al. 2016a; Poggianti et al. 2016), but recently also using radio continuum (e.g. Roberts et al. 2021a; Lal et al. 2022; Roberts et al. 2023, see below). These works enabled to extend the census of ongoing RPS in nearby clusters and to carry out detailed studies of individual galaxies exploiting the now available instrumental capabilities of the integral-field spectrographs (e.g. Merluzzi et al. 2013, 2016; Fumagalli et al. 2014; Fossati et al. 2016, 2019; Consolandi et al. 2017; Poggianti et al. 2017; Bellhouse et al. 2019).

The advent of the new generation radio telescopes has given new impetus to the study of galaxy tails in radio continuum allowing their detection at sensitivities and resolutions which were inaccessible to wide-field radio surveys until now. Through 120-168 MHz radio continuum images from the LOFAR two-meter Sky Survey, Roberts et al. (2021a,b) identified star-forming galaxies (~ 150) with extended asymmetric radio continuum tails likely experiencing RPS in low redshift ($z < 0.05$) clusters and groups. Chen et al. (2020) carried out a 1.4 GHz continuum and HI emission survey in the Coma cluster to investigate the radio properties of RPS galaxies. They detected radio continuum tails in 50% of the targets demonstrating the widespread presence of relativistic electrons and magnetic fields in the stripped tails. Lal et al. (2022) extended the study of the Coma cluster using uGMRT detecting 19 RPS radio continuum tails out of the observed 24 extended radio sources which are cluster members. With the collected uGMRT observations, they were able to derive the spectral structure in all the tailed radio sources. Thanks to the new instrumentation facilities, we can now address the open issues about the nature and origins of the radio tail in RPS galaxies and how the radio continuum emission in the tails correlates with the emission in other

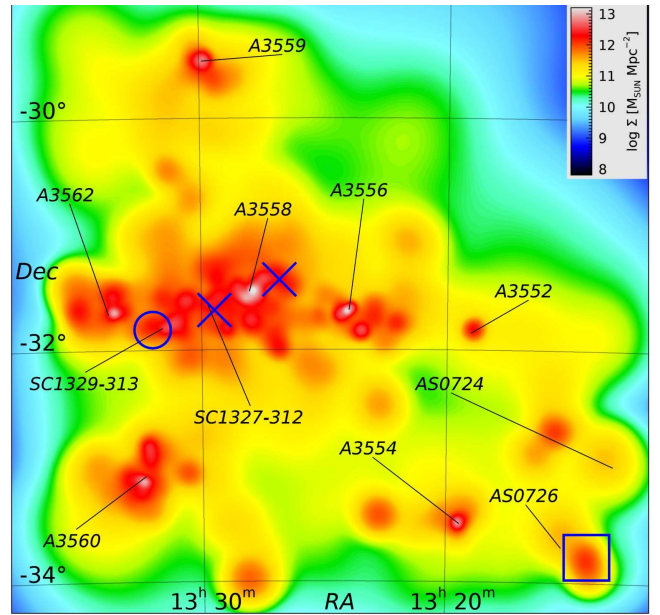


Figure 1. The Shapley Supercluster Survey stellar mass surface density ($M_{\odot} \text{Mpc}^{-2}$) derived from the WISE flux at $3.4 \mu\text{m}$ (Merluzzi et al. 2015). Abell clusters and groups are labeled by black straight lines pointing on the X-ray centre for all systems. Different symbols indicate the positions of the RPS galaxies. SOS 61086 (circle, see Venturi et al. 2022), SOS 90630 and SOS 114732 (crosses, their radio emission is analysed in this work) are covered by ASKAP, MeerKAT, GRMT and uGMRT imaging, while for ShaSS 421 (box, presented in this work), ASKAP imaging only is currently available (see text).

bands and with the galaxy environment. Sophisticated simulations including the effects of either intra-cluster or galaxy magnetic fields are also available (e.g. Ruszkowski et al. 2014; Tonnesen & Stone 2014).

In this framework, the role of the cluster and/or group interactions in triggering the RPS mechanism is debated (see Owers et al. 2012b; Merluzzi et al. 2016; Ebeling & Kalita 2019; Venturi et al. 2022). Deep and high-resolution radio continuum imaging of merging clusters provides, on one side, detailed descriptions of the cluster merger features tracing the intra-cluster diffuse non-thermal emission, on the other side, it reveals the radio continuum tail of individual galaxies. This allows us to investigate the cause-effect relationship, i.e. the link between the large-scale mass assembly and the involved galaxies.

Superclusters are the most massive structures in the Universe ($10^{15} - 10^{16} M_{\odot}$). In such dynamically active and locally dense structures one can potentially observe the effects of dynamical processes such as cluster-cluster collisions and group-cluster mergers and sample different environments from cluster cores to filaments and fields. In the harsh environment of the Shapley supercluster, we have undertaken a search of supercluster members showing radio continuum tails with the aim to investigate if these features are linked with the ongoing or past cluster-cluster interaction.

We report on four radio continuum tails (see Fig. 1) associated to RPS galaxies which are supercluster members and investigate if and to which extent ram-pressure affects the non-thermal component of these galaxies and discuss our results in the light of the ongoing dynamical activity in the Shapley supercluster. The paper is organised as follows. In Section 2 we provide a short description of the selection and properties of the RPS galaxies in our sample. The radio observations and data reduction are described in Section 3 where the

Table 1. Properties of RPS galaxies

Property	SOS 61086	SOS 90630	SOS 114372	ShaSS 421
Coordinates				
ShaSS ¹	13 31 59.80 -31 49 22.2	13 29 28.53 -31 39 25.6	13 26 49.79 -31 23 44.3	13 14 07.43 -33 46 21.1
Magnitudes/fluxes				
$r^{1,2}$	16.29±0.03	16.07±0.03	14.29±0.03	13.97±0.03
24 μ m ³	4007±0.222 mJy	11.013±0.573 mJy	42±2 mJy	
1.4GHz ⁴	0.89 mJy	2.30 mJy	9.31 mJy	
Masses				
stellar mass ^{5,6}	$3.61 \times 10^9 M_{\odot}$	$1.0 \times 10^{10} M_{\odot}$	$7.7 \times 10^{10} M_{\odot}$	$1.6 \times 10^{11} M_{\odot}$
total halo mass ^{5,6}	$1.9 \times 10^{11} M_{\odot}$	$2.5 \times 10^{11} M_{\odot}$	$1.2. \times 10^{12} M_{\odot}$	
Distances				
redshift ⁷	0.04261±0.00023	0.04817±0.00042	0.05152±0.00019	0.05277±0.00015
projected distance ^{5,6}	282 kpc	226 kpc	995 kpc	385 kpc
to the parent cluster centre	$\sim 0.3r_{200}$	$\sim 0.2r_{200}$	$\sim 0.4r_{200}$	$\sim 0.3r_{200}$
Star formation rates				
UV+IR global SFR ³	$1.4 M_{\odot} \text{yr}^{-1}$	$2.5 M_{\odot} \text{yr}^{-1}$	$8.53 M_{\odot} \text{yr}^{-1}$	
H α global SFR ^{5,6}	$1.76 \pm 0.56 M_{\odot} \text{yr}^{-1}$	$3.49 \pm 1.07 M_{\odot} \text{yr}^{-1}$	$7.2 \pm 2.2 M_{\odot} \text{yr}^{-1}$	$6 M_{\odot} \text{yr}^{-1}$

Magnitudes are in the AB photometric system and corrected for galactic extinction.

Sources: ¹Merluzzi et al. (2015); ²Mercurio et al. (2015); ³Haines et al. (2011); ⁴Miller (2005); ⁵Merluzzi et al. (2013) for SOS 114372; ⁶Merluzzi et al. (2018) for SOS 61086 and SOS 90630; ⁷Haines et al. (2018).

radio properties of the galaxies are also derived. In Section 4, complementing the radio observations with multi-band data, we analyse the radio tails in the framework of the RPS scenario. We investigate the origin of the electrons powering the radio tails and highlight the role of the environment in Section 5 and in Section 6 the main results are summarised.

Throughout the paper we adopt a cosmology with $\Omega_M=0.3$, $\Omega_{\Lambda}=0.7$, and $H_0=70 \text{ km s}^{-1} \text{ Mpc}^{-1}$. According to this cosmology 1 arcsec corresponds to 0.96 kpc at the median redshift ($z \sim 0.048$) of the Shapley supercluster. The radio spectral energy distribution is modelled as a power law $S = A\nu^{\alpha}$.

2 RPS GALAXIES IN THE SHAPLEY SUPERCLUSTER

The Shapley supercluster (Shapley 1930) is the most massive supercluster in the local Universe. It encompasses at least 25 Abell clusters in the redshift range $0.035 < z < 0.06$ over a $\sim 15 \times 10 \text{ deg}^2$ region (Raychaudhury 1989; Etori et al. 1997; De Filippis et al. 2005; Proust et al. 2006; Quintana et al. 2020). At the heart of the Shapley supercluster is the high-density Shapley Supercluster Core (SSC, at median redshift $z = 0.048$), comprising three Abell clusters and two poor clusters, forming a continuous filamentary structure 2 deg ($\sim 7 \text{ Mpc}$) in extent filled with hot gas (Planck Collaboration et al. 2013). Evidence of cluster interaction and merging in the SSC were extensively provided by dynamical studies (e.g. Bardelli et al. 1998), X-ray observations (e.g. Finoguenov et al. 2004; Rossetti et al. 2007) and radio continuum analysis (e.g. Venturi et al. 2000, 2003; Giacintucci et al. 2005, 2022). Over the past years, the Shapley Supercluster Survey (ShaSS Merluzzi et al. 2015) traced the filaments feeding the SSC, and revealed how the surrounding clusters are connected to each other and to the SSC (Merluzzi et al. 2015; Haines et al. 2018; Higuchi et al. 2020).

The four galaxies analysed in this work have been identified in the region of the Shapley supercluster covered by the ShaSS by Merluzzi et al. (2013, 2016). From a spectroscopic catalogue, which is 95 per cent complete at magnitude $i < 18$, the RPS candidates were selected in the deep (down to magnitude $r \sim 24$ at 5σ) images collected at the ESO VLT Survey Telescope (VST) according to the criteria introduced by Ebeling et al. (2014): (i) disturbed morphology indicative of a unilateral external force; (ii) brightness knots and colour gradients suggesting bursts of SF; (iii) evidence of tails. The final sample of RPS candidates turned out to constitute the 0.5 per cent of the supercluster galaxies in agreement with the 0.6 per cent found by Ebeling et al. (2014). Among the 13 selected galaxies 9 actually presented extraplanar ionised gas and only 4 turned out to be significantly affected by ram pressure. This does not imply that these are the only galaxies affected by ram pressure across ShaSS, but that the visual selection of the RPS candidates in the ShaSS imaging allowed the identification of these cases (cf. Boselli et al. 2022). All four galaxies are members of the supercluster although associated with different clusters.

Ongoing RPS has been already ascertained for three galaxies (SOS 114372, SOS 90630, SOS 61086) thanks to the observations carried out with the Wide-Field Spectrograph (WiFeS Dopita et al. 2007, 2010), then complemented by N -body/hydrodynamical simulations (see Merluzzi et al. 2013, 2016). The fourth galaxy, ShaSS 421015419 (hereafter ShaSS 421) has been observed with MUSE - Multi-Unit Spectroscopic Explorer (Bacon et al. 2010). The analysis of this particular object is in progress and it will be published in detail elsewhere (Merluzzi et al., in preparation), however there is evidence that this galaxy is also affected by RPS as shown by the preliminary results presented here. Therefore for sake of completeness, we include this object in the sample.

In Table 1 the main global properties of each galaxy are listed. In Fig. 1 the positions of the four galaxies across the ShaSS are indicated together with those of the clusters of galaxies.

Table 2. Logs of the radio observations

Frequency MHz	Array	Project ID	Obs. date	Bandwidth MHz	Time hr	Resolution arcsec×arcsec	rms mJy/beam
235	GMRT	30_024	22-05-2016	32	7	24.45×10.77	0.76
325	GMRT	22_039	30-06-2012	32	7	14.05× 9.53	0.13
400	uGMRT	42_019	06-06-2022	200	7	8.17× 4.78	0.028
400	uGMRT	42_019	10-06-2022	200	7	8.05× 4.51	0.028
610	GMRT	22_039	02-05-2015	32	5	9.54× 5.04	0.11
887	ASKAP ^a	ESP 20	19-03-2019	288	11	13.23×10.43	0.026
943	ASKAP ^b	SB43137	03-08-2022	288	10	18.00×18.00	0.025
1283	MeerKAT	MGCLS ^c	06-08-2018	856	8	7.66× 7.28	0.007
1367	ASKAP ^b	SB43206	06-08-2022	288	8	10.90× 7.80	0.033

a: EMU Evolutionary Map of the Universe (Norris et al. 2011), Early Science Project ESP 20 (Venturi et al. 2022).

b: POSSUM (Polarization Sky Survey of the Universe’s Magnetism, Gaensler et al. 2010) Pilot 2 survey.

c: Pointing belonging to the MeerKAT Galaxy Cluster Legacy Survey (MGCLS, Knowles et al. 2022).

The radio tail of SOS 61086 has been already studied in Venturi et al. (2022), however, in Section 4.4 we recall the main results for a more comprehensive discussion.

3 RADIO DATA

The galaxies SOS 114372, SOS 90630 and SOS 61086 are covered by several radio observations of the SSC over a frequency range from 235 MHz to 1367 MHz, carried out with a variety of radio interferometers. In particular, the data were collected with *i*) GMRT (Swarup et al. 1991) and uGMRT (Gupta et al. 2017) at 235 MHz, 325 MHz, 400 MHz (Band 3) and 610 MHz; *ii*) MeerKAT (Camilo et al. 2018) at 1.28 GHz; and *iii*) the Australian Square Kilometre Array Pathfinder (ASKAP, Hotan et al. 2021) at 887 MHz (EMU Evolutionary Map of the Universe, Norris et al. (2011), Early Science Project ESP 20, Venturi et al. (2022)), 943 MHz and 1367 MHz as part of the POSSUM (Polarization Sky Survey of the Universe’s Magnetism, Gaensler et al. 2010) Pilot 2 survey. On the other hand, for the galaxy ShaSS 421 only ASKAP imaging at 887 MHz (Early Science Project ESP 20) is available at present. The summary of the observations used in this paper is presented in Table 2. For projects 22_039, 30_024 and 42_019 the parameters of the full resolution images are reported.

The observing details and data reduction strategy concerning projects 30_024, 22_039, ESP 20 and MGCLS (MeerKAT Galaxy Cluster Legacy Survey, Knowles et al. 2022) were provided in Venturi et al. (2022) where the radio tail of galaxy SOS 61086 was also studied. MGCLS images at full resolution (see Table 2) and at the resolution of $15'' \times 15''$ have been used. Beyond the total intensity images, the MGCLS data products provide in-band spectral index (in the range 908-1656 MHz) and full Stokes information.

Project 42_019 consists of 5 uGMRT pointings in Band 3 (250-550 MHz) which cover the SSC from west of the cluster A 3558 to east of A 3562. It was designed to study the diffuse emission features in this region (Trehaven et al. in prep). The two datasets which include SOS 90630 and SOS 114372 are centred at $RA_{J2000} = 13^h 30^m 0^s$ and $DEC_{J2000} = -31^\circ 39' 00''$ and $RA_{J2000} = 13^h 27^m 58^s$ and $DEC_{J2000} = -31^\circ 30' 30''$ for the two sources respectively. The data were recorded with 8192 spectral channels and an integration time of 4 sec in full Stokes mode. The sources 3C 48 and 3C 236 were used as primary calibrators, and 1311–222 was used as phase calibrator. The data were processed by means of SPAM (Source

Peeling and Atmospheric Modelling, Intema et al. 2009). The full band was split into 6 sub-bands each 33.3 MHz wide and the sub-band were then imaged together using WSClean (v2.10) at the common frequency of 400 MHz. Residual amplitude errors are of the order of 8%. The final deep images were produced with *weighting='Briggs'* using *robust=-0.5* and a set of tapering to properly image the features on different angular scales. Primary beam correction was performed using the task PBCOR in the NRAO Astronomical Image Processing System (AIPS).

All galaxies discussed in this paper (SOS 61086, SOS 90630, SOS 114372 and ShaSS 421) are included in the $\sim 6 \times 6$ deg² field imaged by ASKAP at 887 MHz as part of the EMU Early Science Programme (Johnston et al. 2008; Norris et al. 2011) ESP 20 and already presented in Venturi et al. (2022), where observation and data reduction details are given. In brief, the telescope was configured to produce 36 electronically formed beams arranged on the sky in a 6×6 square grid; each individual beam covers an area of ~ 1 deg² for a total instantaneous field of view of ~ 31 deg². The observations were performed with 35 out of the 36 antennas of the array, at 887 MHz, with bandwidth $\Delta\nu=288$ MHz (288 channels each of bandwidth of 1 MHz). The final image is centred at $RA_{J2000} = 13^h 25^m 50^s$, $DEC_{J2000} = -31^\circ 03' 05''$. Residual amplitude calibration errors are of the order of 5%.

Finally, the galaxies SOS 61086, SOS 90630, SOS 114372 were observed by ASKAP as part of the POSSUM Pilot 2 survey (POSSUM2), whose goal is to study the magnetic fields of the Universe in different environments. The pointing centres for Band 1 (800-1088 MHz) and Band 2 (1152-1440 MHz) are respectively $RA_{J2000} = 13^h 29^m 47^s$ and $DEC_{J2000} = -30^\circ 17' 10''$ and $RA_{J2000} = 13^h 28^m 51^s$ and $DEC_{J2000} = -29^\circ 43' 04''$. The Band 1 data was taken in the *closepack36* PAF beam configuration and Band 2 was in the *square_6x6* configuration. Due to the different frequencies, the final image in Band 2 covers a slightly smaller sky area, each of the electronically formed beam being $\sim 30\%$ smaller than in Band 1. The data reduction of the POSSUM2 observations is the same as the procedure followed for the Rapid ASKAP Continuum Survey (RACS), detailed in Duchesne et al. (2023). Residual amplitude calibration errors are of the order of 5%. The datasets in both bands provide total intensity images, polarisation information through Rotation Measure (RM) synthesis, and spectral index information (obtained dividing the Taylor 1 by the Taylor 0 images). The final full resolution images of the galaxies SOS 90630 and SOS 114372 at all radio frequencies

Table 3. Flux density values from images convolved to 18×18 arcsec².

Galaxy	Frequency MHz	Telescope Array	S _{tot} mJy	S _{gal+tail1} mJy	S _{tail2} mJy
SOS 90630	235	GMRT	9.01± 0.90	<i>a</i>	<i>a</i>
	325	GMRT	6.92± 0.63	5.90± 0.59	1.08± 0.19
	400	uGMRT	5.63± 0.47	5.39± 0.43	0.27± 0.07
	887	ASKAP ^b	3.72± 0.20	3.63± 0.18	0.22± 0.03
	943	ASKAP ^c	3.82± 0.20	3.57± 0.18	0.18± 0.03
	1283	MeerKAT	2.89± 0.12	2.68± 0.10	0.12± 0.01
	1367	ASKAP ^c	2.52± 0.15	2.46± 0.13	0.12± 0.04
SOS 114372	235	GMRT	21.93± 3.58	<i>a</i>	<i>a</i>
	325	GMRT	30.56± 2.50	24.77± 2.48	5.88± 0.84
	400	uGMRT	27.13± 2.18	22.64± 1.81	5.70± 0.49
	887	ASKAP ^b	16.70± 0.84	14.39± 1.44	2.86± 0.16
	943	ASKAP ^c	15.82± 0.80	13.88± 1.39	2.16± 0.13
	1283	MeerKAT	11.67± 0.47	10.35± 1.04	1.42± 0.11
	1367	ASKAP ^c	11.09± 0.57	9.54± 0.48	1.18± 0.10

a: See Section 3.1.

b: EMU Evolutionary Map of the Universe (Norris et al. 2011), Early Science Project ESP 20 (Venturi et al. 2022).

c: POSSUM (Polarization Sky Survey of the Universe’s Magnetism, Gaensler et al. 2010) Pilot 2 survey.

are reported in the Appendix A. The analysis of the polarisation will be presented in a forthcoming paper.

3.1 Radio images and fluxes

Our aim is to investigate the nature of the extraplanar radio continuum emission, i.e. to identify the mechanisms responsible of such a feature as well as which processes are powering the electrons outside the galaxy disk. The multi-band radio data with their resolution and sensitivity enable us to derive the radio properties in different regions - discs and tails. However, the different angular resolutions in our dataset (see Table 2) need to be considered in defining the galaxy regions. For SOS 90630 and SOS 114372, we can distinguish two regions: one comprehending the galaxy and the inner part of the tail (hereafter ‘gal+tail1’) and the other covering the outer part of the tail (tail2). This choice was made to account for the different angular resolutions of our radio images.

For SOS 90630 in Fig. A1 we notice that in the full resolution images the length of the tail is similar (~ 43 kpc) at four frequencies, while at 235, 610 and 1367 MHz the sensitivities do not (or only barely) allow the detection of the radio tail outside the visible galaxy (see Table 2).

In Fig. A2 the tail of SOS 114372 shows, at the sensitivity of our images, different extensions in projection at different frequencies, e.g. ~ 72 kpc at 943 MHz and 29 kpc at 1367 MHz. We notice that the ASKAP-POSSUM2 image at 943 MHz has the second better sensitivity in the dataset and traces the extraplanar emission further out the galaxy disk.

To account for the different angular resolutions in our datasets, which range from $7.66'' \times 7.28''$ of the full-resolution MeerKAT images to $18'' \times 18''$ for ASKAP-POSSUM Band 1, and ensure a consistent spectral analysis, we convolved all images to the same angular resolution of $18'' \times 18''$, with the exception of GMRT 235 MHz for SOS 90630 (whose beam is larger) and GMRT 610 MHz (which is not used in the analysis, see below). The convolved images are shown in Figs. A3 and A4.

At each frequency, for SOS 90630 and SOS 114372 we derived *i*)

the integrated flux density; *ii*) the flux density of gal+tail1; *iii*) the flux density of the remaining outer part of the tail (tail2). At the adopted resolution the gal+tail1 component is all included within the beam of the image, and S_{gal+tail1} has been obtained fitting the peak in the image with a Gaussian component (see Fig. 2). The total flux, S_{tot}, was derived by integration over the whole area taking the images at 943 MHz as reference. The flux of tail2 is obtained subtracting S_{gal+tail1} from S_{tot}. These values are listed in Table 3.

For each galaxy and each component we estimated the uncertainty ΔS on the flux density S using the relation

$$\Delta S = \sqrt{(\sigma \times \sqrt{N_{\text{beam}}})^2 + (\xi_{\text{cal}} \times S)^2} \quad (1)$$

where σ is the local noise in the image, N_{beam} is the extent of the source (or component) in number of beams, ξ_{cal} is the calibration uncertainty.

For ShaSS 421 we derived S_{tot}=5.16±0.26 mJy. All the other flux density values are reported in Table 3.

In the following we provide a description of the radio morphology for each galaxy and a zero-order analysis of the integrated spectrum of the region encompassing the galaxy and the beginning of the radio tail (gal+tail1), and of the outer tail region (tail2). In the description of the morphology we benefit of the high-resolution MeerKAT images, although the quantitative analysis is based on the convolved images.

SOS 90630. This galaxy shows a radio continuum tail oriented westwards with respect to the position of the optical galaxy centre, coincident with the radio peak. At 1.28 GHz it extends for 45 arcsec (~ 43 kpc) with hints that the radio tail forks in two branches perpendicular to the direction of the tail at 40 arcsec west from the centre, as seen in the MeerKAT 1283 MHz image at full resolution (Fig. 3). We point out that the westernmost knot is most likely associated with the background galaxy visible in Fig. 3 and for this reason we do not consider it as part of the tail. The total radio power of SOS 90630 at 1367 MHz is $P_{1367\text{MHz}} = 1.49 \times 10^{22} \text{ W Hz}^{-1}$.

In order to check for spectral steepening along the tail, we separated

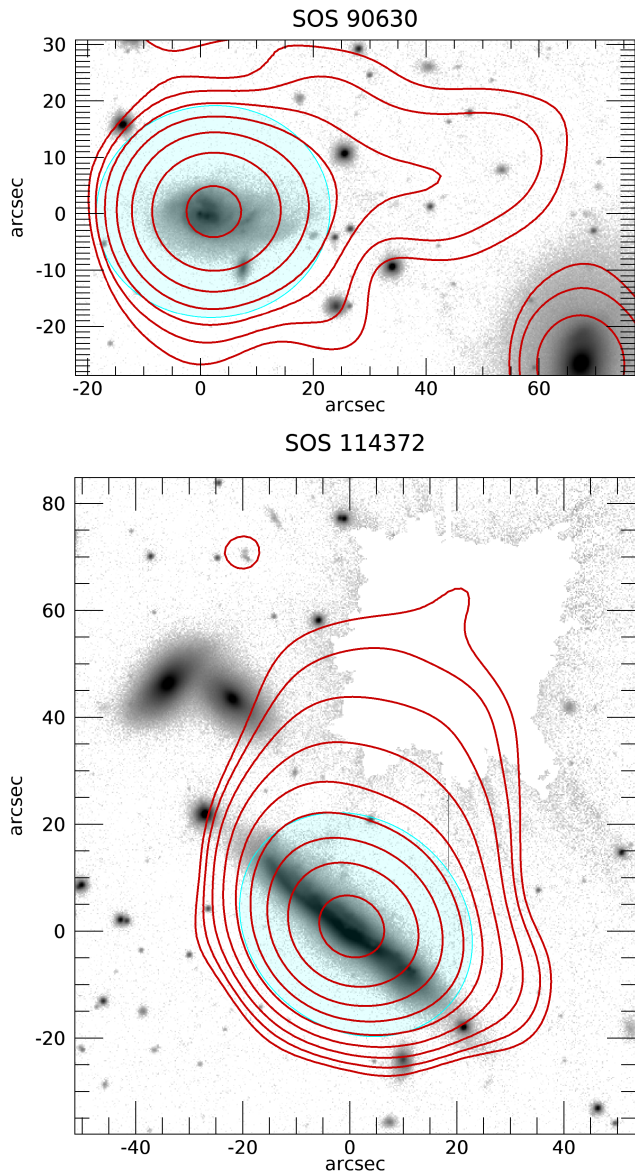


Figure 2. VST r -band images with superimposed the 1.28 GHz MeerKAT isophotes convolved to $18 \times 18 \text{ arcsec}^2$ of SOS 90630 (upper panel) and SOS 114372 (lower panel). The cyan regions denote the fitted Gaussian component (see text) up to $r=1 \times \text{FWHM}$. The radio contours are spaced by a factor 2 in flux.

the flux density of the radio emission in the two components as explained above. Using the flux density obtained from the $18'' \times 18''$ images for each component we fitted the spectra of these two components with a power law (the 610 MHz flux density values were not included in the fit as they are clearly overestimated). Despite the scatter of our measurements along the tail, mainly due to the different radio interferometers used in this analysis, our data show an unambiguous steepening, with $\alpha_{325 \text{ MHz}}^{1367 \text{ MHz}}(\text{gal}+\text{tail}1) = -0.63 \pm 0.11$ and $\alpha_{325 \text{ MHz}}^{1367 \text{ MHz}}(\text{tail}2) = -1.03 \pm 0.12$. The integrated spectrum of the radio emission has a spectral index $\alpha_{235 \text{ MHz}}^{1367 \text{ MHz}}(\text{tot}) = -0.62 \pm 0.09$.

SOS 114372. The radio emission in this galaxy follows the optical disc (but see Section 4.2), for a total size of $\sim 30 \text{ kpc}$, and is characterised by a radio tail roughly perpendicular in projection to

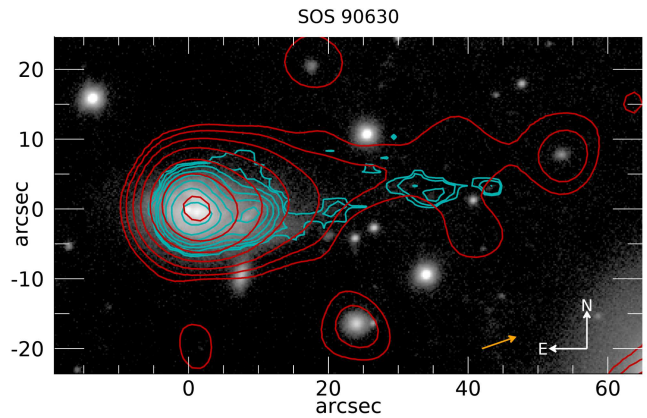


Figure 3. VST r -band image of SOS 90639 ($\sim 0.6''$ angular resolution) with superimposed the 1.28 GHz MeerKAT radio contours (red, $7''$ angular resolution) and the $H\alpha$ contours (cyan, $\sim 1.5''$ angular resolution). The radio outer isophote corresponds to 3σ (0.021 mJy b^{-1}), the subsequent isophotes are spaced by a factor 2 in flux. For the $H\alpha$ data from WiFeS, the outer isophote corresponds to $5 \times 10^{-18} \text{ erg s}^{-1} \text{ arcsec}^{-2}$ (5σ in WiFeS spectra), the other isophotes are spaced by a factor 2 in flux. Bottom right: the orientation of the field and the direction of the wind velocity (orange arrow, see text) are indicated.

the optical disc in the north-west direction, as shown in Fig. 4. The radio tail is resolved along its minor axis, and shows two ridges of emission extending $\sim 40 \text{ arcsec}$ ($\sim 38 \text{ kpc}$) north of the disc, clearly visible at all frequencies in the higher resolution images. The total radio power at 1367 MHz for this source is $P_{1367 \text{ MHz}} = 6.35 \times 10^{22} \text{ W Hz}^{-1}$.

As in the case of SOS 90630, using the flux density values derived from the $18'' \times 18''$ images a single power law fit shows a clear spectral steepening in tail2 compared to the combination of the galaxy and beginning of the tail. In particular, we measured $\alpha_{325 \text{ MHz}}^{1367 \text{ MHz}}(\text{gal}+\text{tail}1) = -0.72 \pm 0.10$ and $\alpha_{325 \text{ MHz}}^{1367 \text{ MHz}}(\text{tail}2) = -1.49 \pm 0.12$. The integrated spectrum of the radio emission is dominated by the galaxy and has a spectral index $\alpha_{325 \text{ MHz}}^{1367 \text{ MHz}}(\text{tot}) = -0.70 \pm 0.10$.

ShaSS 421. Only the 887 MHz ASKAP observation is available for ShaSS 421. No radio tail is detected at the sensitivity of the image, whose local noise is $\sim 50 \mu\text{Jy b}^{-1}$, significantly higher than for SOS 90630 and SOS 114372. The radio emission extends for $\sim 62 \text{ kpc}$ along the optical disc, as shown in Fig. 5. The radio morphology has a bipolar shape. The radio continuum emission detected by ASKAP peaks in the centre of the galaxy stellar disc. Moving away from the centre along the galaxy major axes in both sides of the disc, the radio emission shows recollimation, to broaden again in a ‘wrapped candy’ morphology. The radio power of the emission is $P_{887 \text{ MHz}} = 3.45 \times 10^{22} \text{ W Hz}^{-1}$. The radio morphology is actually suggestive of a radio galaxy of nuclear origin. We extracted the 1.4 GHz flux density from the NRAO VLA Sky Survey (NVSS, Condon et al. 1998) and obtained a total spectral index $\alpha_{887 \text{ MHz}}^{1400 \text{ MHz}} = -1.04 \pm 0.18$. Further studies on the origin of the radio emission are ongoing.

4 RADIO TAILS OF RPS GALAXIES

In this section we analyse the observed radio properties of SOS 90630, SOS 114372 and ShaSS 421 in the framework of the RPS scenario as supported for these objects by multi-band studies

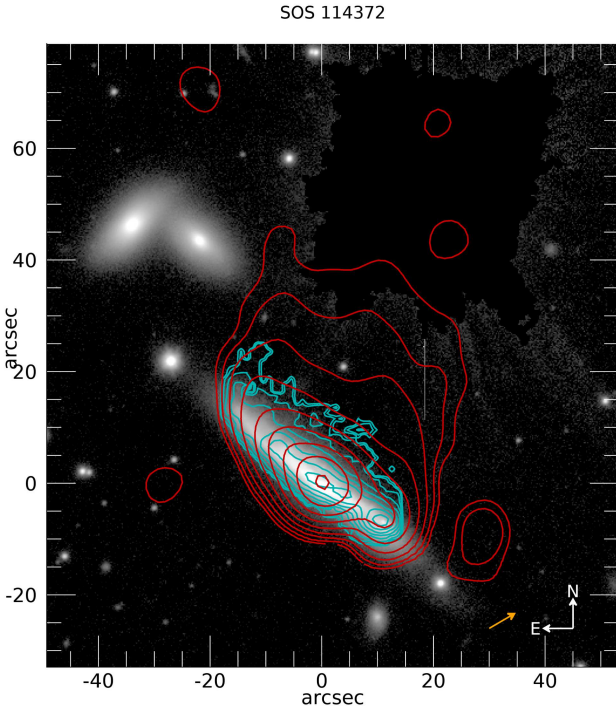


Figure 4. VST r -band image of SOS 114372 ($\sim 0.6''$ angular resolution) with superimposed the 1.28 GHz MeerKAT radio contours (red, $7''$ angular resolution) and the $H\alpha$ contours (cyan, $\sim 1.5''$ angular resolution). The contours are drawn as in Fig. 3. Bottom right: the orientation of the field and the direction of the wind velocity (orange arrow, see text) are indicated.

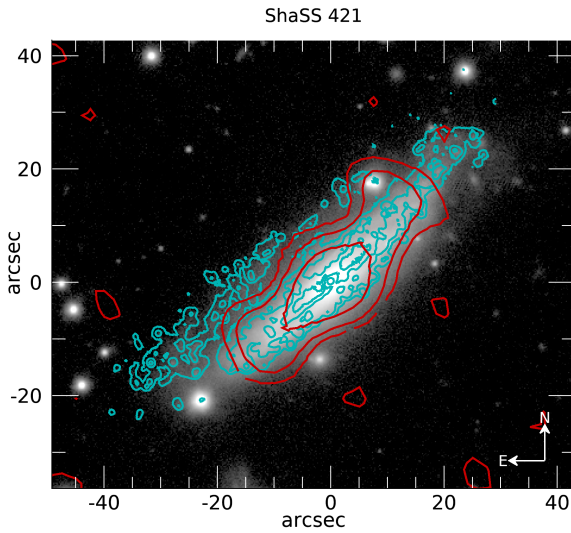


Figure 5. VST r -band image of ShaSS 421 ($\sim 0.6''$ angular resolution) with superimposed the ASKAP contours (red, restoring beam $13.2'' \times 10.4''$). The radio outer isophote corresponds to 3σ (0.15 mJy b^{-1} , here we adopted the local noise since the galaxy is close to the image border), the subsequent isophotes are spaced by a factor 2 in flux. For the $H\alpha$ data from MUSE (cyan), the outer isophote corresponds to $1 \times 10^{-18} \text{ erg s}^{-1} \text{ arcsec}^{-2}$, the other isophotes are spaced by a factor 4 in flux.

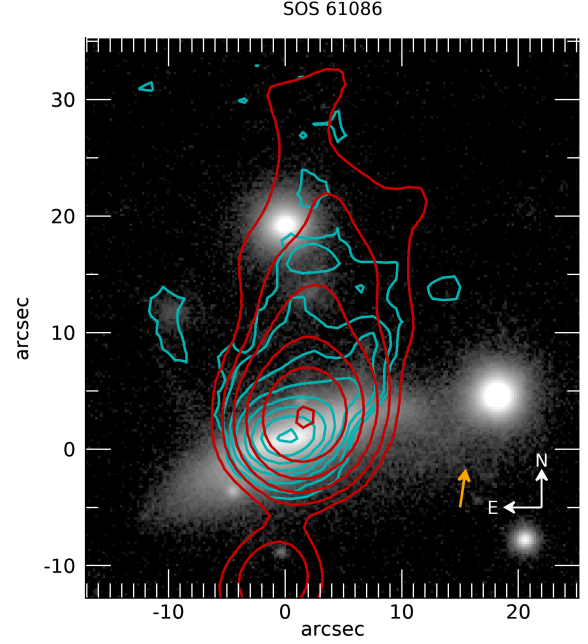


Figure 6. VST r -band image of SOS 61086 ($\sim 0.6''$ angular resolution) with superimposed the 1.28 GHz MeerKAT radio contours (red, $7''$ angular resolution) and the $H\alpha$ contours (cyan, $\sim 1.5''$ angular resolution). The contours are drawn as in Fig. 3. Bottom right: the orientation of the field and the direction of the wind velocity (orange arrow, see text) are indicated.

and hydrodynamical simulations. We also recall the main results obtained by Venturi et al. (2022) for SOS 61086. In Figs. 3, 4, 5 and 6 we show the VST r -band image of each galaxy with superimposed the radio continuum emission at 1.28 MHz (red contours) and the $H\alpha$ emission (cyan contours).

4.1 SOS 90630

The galaxy SOS 90630 is a member of the poor cluster SC 1327-312. The VST r -band image Fig. 3 shows the highly asymmetric light distribution with a western arm extending well out of the disc. The deep MeerKAT radio continuum emission at 1.28 MHz peaks at the galaxy centre and extends west in the same direction of the asymmetric emission observed in the visible image.

To estimate the equipartition magnetic field for the galaxy and inner tail (gal+tail1) and for the outer part of the tail (tail2) we used the formulae in Govoni & Feretti (2004). For both regions we assumed a cylindrical volume, a ratio between electrons and protons $k=1$ and a filling factor $\Phi=1$, obtaining $H_{\text{eq}} \sim 1.8 \mu\text{G}$ and $\sim 0.9 \mu\text{G}$, respectively.

In order to estimate the age of the radiating electrons in the two regions under considerations, we derived the break frequency ν_{br} by fitting the synchrotron spectrum with the software Synage (Murgia et al. 1999). The best fit is obtained assuming a JP model (Jaffe & Perola 1973) and an injection spectral index $\alpha_{\text{inj}} = -0.5$. The fit provides a break frequency $\nu_{\text{br}} = 10327 \text{ MHz}$ for gal+tail1, and $\nu_{\text{br}} = 1994 \text{ MHz}$ for tail2. The fit of the radio emissions are shown in Fig. B1, upper row. The corresponding radiative ages, computed following Eq. 1 in Feretti et al. (1998) which accounts for the equivalent magnetic field strength of the CMB radiation, are $t_{\text{rad}} \sim 4.0 \times 10^7 \text{ yr}$ for the galaxy and inner tail and $t_{\text{rad}} \sim 7.7 \times 10^7 \text{ yr}$ for the outer tail.

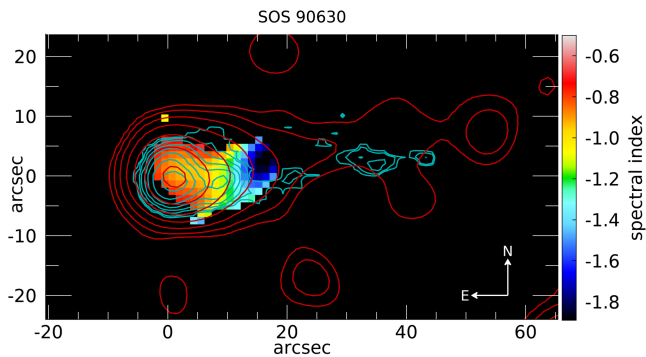


Figure 7. The MeerKAT inband spectral index in the frequency range 908-1656 MHz. Red and cyan contours denote the radio continuum and H α emission, respectively. The MeerKAT spatial resolution is $7.66'' \times 7.28''$ (p.a. 68.17). The contours are drawn as in Fig. 3.

The MeerKAT inband spectral index in the frequency range 908-1656 MHz could be derived only for the nuclear component and inner part of the tail. The surface brightness in the region corresponding to tail2 is too low and falls below the sensitivity limit of each frequency channel used to derive the inband spectral index. Fig. 7 clearly shows the steepening from the nuclear region, where the spectral index is $\alpha \sim -0.8$, out to the edge of tail1 where $\alpha \sim -1.8$.

In Fig. 3 we also show the distribution of the H α emission from WiFeS IFS (cyan contours) as analysed by Merluzzi et al. (2016). The gas out of the disc extends ~ 4 kpc in projection in the NW side, and along a more than 40 kpc-long tail to the west. The radio tail extends in projection with almost the same length. The ionised gas disc is also truncated in the South-East side. Due to the different resolution it is not clear if the non-thermal emission of the galaxy is characterised by a similar truncation. Moreover, the moderate disc truncation observed in the ionised gas distribution could be related to the galaxy inclination angle whose impact on the amount of gas stripped from a disc is significant when the wind is close to edge-on as was shown with hydrodynamical and numerical simulations (e.g. Roediger & Brüggén 2006; Jáchym et al. 2009). In this case much less gas is removed from the galaxy reducing the truncation effect.

Merluzzi et al. (2016) found that the star formation across SOS 90630 is highly asymmetric with a ‘crown’ of HII regions tracing the eastern disc and other star-forming regions in the western disc elongated toward the tail in a spiral arm (see their Fig. 17 and Abramson & Kenney 2014).

A single burst of star formation over the last 200 Myr that is still ongoing is responsible of the young stellar population detected in the centre and in the eastern edge of the galaxy disc, which is likely induced by the compression exerted by the ram pressure. Due to their ageing as traced by the inband spectral index in Fig. 7, the electrons in the inner tail can be originated by this ongoing star formation.

N -body/hydrodynamical simulations (see Appendix C and Merluzzi et al. 2016, for details) enabled to estimate the parameters of the hydrodynamical interaction between the gas disc of the galaxy and the ICM of host cluster SC1327-312 indicating a ram pressure acting close to edge-on, a wind velocity $V_{ICM} = 500 \text{ km s}^{-1}$ and the time of the ram-pressure onset of about 120 Myr.

Together with the similar length of the radio tail and the ionised gas tail, the consistency among *i*) the epoch of the onset of stripping (120 Myr); *ii*) the age of the youngest stellar population (< 200 Myr) and *iii*) the age of the radio tail (< 100 Myr) supports a scenario where the radio emitting plasma and the warm gas tails are related

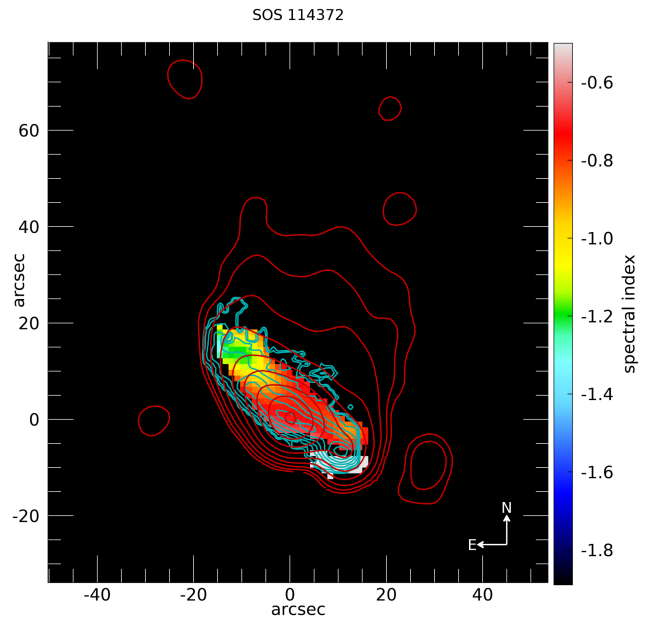


Figure 8. The MeerKAT inband spectral index of SOS 114372 in the frequency range 908-1656 MHz. Red and cyan contours denote the radio continuum and H α emission, respectively. The MeerKAT spatial resolution is $7.66'' \times 7.06''$ (p.a. 1.21). The contours are drawn as in Fig. 3.

to the same event, i.e. both affected by the ram pressure with similar efficiency (cf. the Virgo galaxy NGC 4438, Vollmer et al. 2009).

4.2 SOS 114372

The bright star-forming spiral galaxy SOS 114372 is the only galaxy of the sample which is member of a rich cluster, A 3558. Extraplanar ionised gas has been detected along the full extent of the galaxy disc out to 13 kpc in projection from it (cyan contours in Fig. 4). Running N -body/hydrodynamical simulations of RPS for this galaxy (see Appendix C), Merluzzi et al. (2013) reproduced the observed distribution and surface brightness of the ionised gas. In this case, the wind angle turns out to be intermediate between face-on and edge-on, the estimated wind velocity is $\sim 1400 \text{ km s}^{-1}$ and the derived time of onset of the RPS is $t \sim 60$ Myr.

MeerKAT observations reveal a widespread emission out of the galaxy disc whose extension in projection largely overcomes (38 kpc long at 1.28 MHz) the ionised gas tail. In this case the truncated ionised gas disc observed in the NE edge of the galaxy corresponds to a clear truncation also in the radio continuum (see Fig. 4). We point out that the IFS observations do not cover the whole galaxy, for the SW edge of the galaxy IFS data are not available (see the sharp end of the cyan contours line in Fig. 4 and Fig. 1 of Merluzzi et al. 2013). Therefore, it is misleading to compare radio and IFS observations in this part of the galaxy.

We computed the equipartition magnetic field and estimated the radiative age of the electrons in the gal+tail1 and in the outer part of the tail (tail2) under the same assumptions used for SOS 90630. We obtained $H_{eq} \sim 2.56 \mu\text{G}$ and $0.86 \mu\text{G}$ respectively. We fitted the spectra of the two regions as for SOS 90630. Again the best fit was provided by a JP model (see Fig. B1, lower row). We derived $\nu_{br} = 6851 \text{ MHz}$ and $\nu_{br} = 1428 \text{ MHz}$ for gal+tail1 and tail2, respectively, with a corresponding age for the radiating electrons of $t_{rad} \sim 4.8 \times 10^7 \text{ yr}$ and $t_{rad} \sim 9.3 \times 10^7 \text{ yr}$.

The MeerKAT inband spectral index, shown in Fig. 8 with radio continuum and $H\alpha$ contours overlaid, covers only the disc of the galaxy. It is flat in the internal disc and consistent with the estimate of the spectral index of the integrated spectrum throughout the whole extent of the disc. We notice, however a marginal steepening at the north-eastern edge of the disc and a region characterised by the higher values of the spectral index SW in the disc. Unfortunately, due to sensitivity limits, the inband spectral index along the tail could not be derived.

In a region SW from the centre Merluzzi et al. (2013) identified a starburst. The agreement between the age (~ 100 Myr) of the youngest stellar population in this region and the age (started ~ 60 Myr ago) of the gas stripping process inferred by the N -body/hydrodynamical simulations led to ascribe this starburst to the compression of the ISM caused by the ram pressure - one of the first detections of ram-pressure induced star formation. On the other hand, in the NE disc a region of star formation significantly lower than in the rest of the disc was also identified. The full spectral modelling and the line strengths provided evidence for the detection of a starburst which lasted for ~ 0.3 Gyr and which has been just shut down. It is remarkable that these two regions correspond to the regions where the extreme values of the radio spectral index are measured in the disc as shown in Fig. 8, i.e. the spectral index steepens in the post-starburst NE region and flattens in the SW starburst region of the disc. This shows how the 1.28 MHz MeerKAT observations are able to resolve the star formation in the Shapley Supercluster galaxies.

The flatness of the spectral index towards the SW starburst region is consistent with the decreasing trend of the spectral index with increasing SFR found in nearby galaxies covering a wide range in morphology, SFR, stellar mass, and environment (field vs. interacting galaxies) studied with both global (e.g. Tabatabaei et al. 2017) and spatially resolved measurements (e.g. Westcott et al. 2018). This suggests that the star-formation process could affect the energetics of the cosmic-ray electron population in a galaxy by increasing the number of younger and more energetic relativistic particles in galaxy regions with higher star-formation activity (e.g. starburst).

Also for this object the consistency among *i*) the epoch of the onset of stripping (~ 60 Myr); *ii*) the age of the youngest stellar population (< 100 Myr) and *iii*) the age of the radio tail (< 100 Myr) suggest that the relativistic electrons and the ionised gas are both stripped from the disc by the same mechanism. However, unlike SOS 90630, the length of the radio and optical tails are significantly different.

4.3 ShaSS 421

ShaSS 421 is the brightest and most massive galaxy of the sample. A detailed study of this object, based on MUSE observations, is in preparation. Here we briefly mention the main features supporting the ongoing RPS scenario.

Fig. 5 shows evidence of extraplanar ionised gas extending NE from the disc. Within a radius ~ 250 kpc there are not other cluster members with signs of disturbed morphology, therefore excluding galaxy interaction as the cause of the observed extraplanar emission. Further evidence in favour of the RPS scenario is given by the orientation of the ShaSS 421 tail which is opposite to the peak of galaxy density as derived in the ShaSS (Merluzzi et al. 2015; Haines et al. 2018). The galaxy is located ~ 385 kpc in projection ($0.3r_{200}$) from the centre of AS 0726 as shown in Fig. 9.

The galaxy was targeted with MUSE. Two contiguous pointings slightly overlapped in the centre covered an area of $\sim 1' \times 2'$ including the galaxy and its extraplanar region. In Fig. 5 the ionised gas emission traced by $H\alpha$ is shown. The extraplanar gas extends NW up

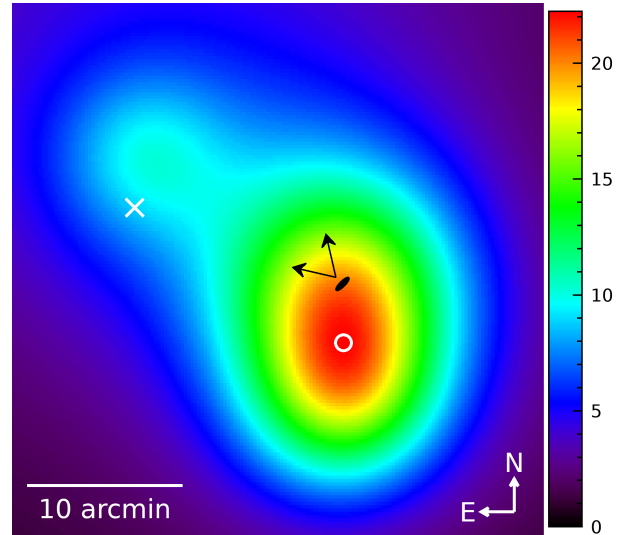


Figure 9. The two-dimensional distribution of SSC galaxies in the region of AS 0726 (from Haines et al. 2018). The small circle indicate the peak of the galaxy density. The small black ellipse north from this peak shows the galaxy (on scale) with the arrows indicating the range of directions of the gas outflow. The cross is the ROSAT X-centre by De Filippis et al. (2005). The density scale is in galaxies per Mpc^2 .

to 15 kpc out of the disc and along all the disc length. The one-sided extraplanar gas emission as well as the truncation of the gas disc along the SW edge of the galaxy support an ongoing RPS event.

In this galaxy, we do not observe a radio tail. The analysis of the MUSE spectra showed that the galaxy host an AGN which could be responsible of the radio emission intensity and shape. However, the extent of the $H\alpha$ emission is larger than the radio emission, which does not reach either the outer edges of the galaxy or the south-eastern extent above the galaxy disc. It seems that the RPS mechanism is not capable to affect the non-thermal component of this galaxy.

4.4 SOS 61086

The radio tail of SOS 61086 has been studied in Venturi et al. (2022). Here we recall the main features of this object and the proposed interpretation in order to compare them with those of the other galaxies in the sample.

SOS 61086 is a member of the poor cluster SC 1329-313. Merluzzi et al. (2018) showed that this galaxy is characterised by a tail of ionised gas extending up to ~ 30 kpc in projection. They demonstrated that the galaxy is affected by RPS and estimated the time of the onset ('age') of RPS of about 250 Myr in agreement with the age of the young stellar population (< 200 Myr), which likely suggests a ram-pressure induced star formation.

Venturi et al. (2022) reported on the radio tail revealed at 1.28 MHz with MeerKAT. The radio-emitting plasma and the ionised gas show equal extent in projection from the galaxy disc and similar truncation in the gas disc itself (see Fig. 6). Taking into account the steepening of the radio spectral index along the tail, the age of the relativistic electrons and their velocity, which is found to be consistent with the wind velocity inferred from the N -body/hydrodynamical simulation, Venturi et al. (2022) concluded that the radio tail revealed by MeerKAT observations in SOS 61086 is due to the ongoing RPS and it is fuelled by relativistic electrons stripped from the galaxy.

5 DISCUSSION

In Section 4, we provide evidence that the ionised gas tail and that traced by the relativistic electrons are due to the same mechanism - the hydrodynamical interaction between the ICM and the ISM. A step further is to understand if the radio continuum emission in the tail is powered either by *in situ* star formation (Gavazzi et al. 1995) or by relativistic electrons stripped from the galaxy by ram pressure and possibly re-accelerated (Chen et al. 2020).

Among the four RPS galaxies showing ionised gas tails, three present consistent synchrotron tails revealed by multi-frequency radio observations, while the 887 MHz ASKAP observations do not detect radio continuum extraplanar emission in the most massive galaxy of the sample, ShaSS 421. Beyond the different instrumental characteristics (sensitivity and spatial resolution), which are crucial for the detection of the faint extraplanar emission, the galaxy properties and orbits as well as their own environment may play an important role in the process of sweeping away the ISM from the disc.

In the following we investigate the origin of the electrons in the tail and describe the different environments of the RPS galaxies in our sample also in order to possibly distinguish the effects of the magnetic field in the RPS process.

5.1 Origin of the relativistic electrons in the tail of SOS 90630

The relative lengths of the radio continuum emission and the $H\alpha$ tails can provide a piece of information to disentangle the origin of the relativistic electrons in the tail. Radio tails either longer (e.g. Gavazzi et al. 1995) or shorter (e.g. Chen et al. 2020) than $H\alpha$ ones have been observed. However, it is difficult to compare the lengths of the tails because differences in extent may be due on differences in sensitivity and projection effects.

The velocity of the plasma containing the relativistic electrons stripped from the galaxy can be estimated from the tail length and the radiative age. The age estimated for the relativistic electrons (~ 77 Myr) in tail2 is actually an average value throughout the extent of the tail which can be associated to the average distance from the centre of the outer tail, i.e. 30 kpc (see Fig. 2). The tail length should be then corrected for the projection effect using the angle between the ram-pressure wind velocity, as derived by the simulations, and the line of sight. In this case this angle is $\phi \sim 67$ deg.

Under these assumptions, we obtain a velocity of the stripped non-thermal component of $\sim 420 \text{ km s}^{-1}$, which is consistent with the wind velocity ($V_{ICM} = 500 \text{ km s}^{-1}$) resulting from the N -body/hydrodynamical simulations of RPS affecting SOS 90630. The result indicates that the radio tail is produced by the gas stripped from the disc.

The other piece of information is given by the radio spectral index across the galaxy and the tail. Also in this case, opposite behaviours have been reported in the literature for different objects. Vollmer et al. (2009) did not observe a steepening of the spectral index in the extraplanar radio emission of NGC 4438, while other studies (Vollmer et al. 2004b; Chyży et al. 2006; Chen et al. 2020) reported a rapid ageing of the electrons with increasing distance from the galaxy disc. For SOS 90630 we actually observe a steepening in the inband spectral index (Fig. 7) which denotes an electron ageing from the galaxy disc to the inner tail thus supporting that the relativistic electrons are, at least in the inner tail, stripped from the galaxy disc. Also considering the spectra of gal+tail1 and tail2 (see Section 3.1) we measure a clear steepening of the spectral index in tail2 although corresponding to only a modest ageing.

However, we notice that the line diagnostics analysis shows that the excitation of the gas both within the main body of the galaxy and within its extended tail is due to HII regions (Merluzzi et al. 2016). Therefore, even if we tend to interpret the radio emission of the tail as due to electrons stripped from the galaxy disc, in the outer tail we cannot exclude a contribution due to *in situ* star formation, which would account for the modest ageing observed in this region.

5.2 Origin of the relativistic electrons in the tail of SOS 114372

The spectra of gal+tail1 and tail2 (see Section 3.1) show a steepening of the spectral index in tail2 which suggests that the relativistic electrons origin from the galaxy disc. The ageing observed in tail2 is nevertheless not dramatic. Merluzzi et al. (2013) showed that the emission in some regions of the galaxy and in the whole gas outflow presents a significant contribution from shock excitation, together with emission powered by star formation. The distribution of the regions with higher velocity dispersion and shock-ionised gas across the galaxy shows that the ram pressure compresses and strips the gas out of SOS 114372, forming a tail of turbulent shock-ionised gas and dust (Merluzzi et al. 2013). Shock due to ram pressure may similarly affect and accelerate also the relativistic electrons (e.g. Vollmer et al. 2004a) and explain their modest ageing in the outer tail.

Although the difference in length of the radio and $H\alpha$ tails may depend to difference in sensitivity, the almost $3\times$ longer radio tail of SOS 114372 deserves further investigations.

A more extended tail in radio than $H\alpha$ could be consistent with similar results found in galaxies and explained in terms of different time-scales involving star formation traced by the two emissions (e.g. Leslie et al. 2017). While radio emission traces star formation on time-scales > 10 Myr, $H\alpha$ emission traces star formation on smaller time-scales. Leslie et al. (2017) found that the older star formation traced by the 1.4 GHz emission is more extended than the younger one traced by the $H\alpha$ emission on a sample of star-forming galaxies. Since our highest radio frequencies (1283-1367 MHz, see Table 2) are very close to the canonical radio tracer of star formation at 1.4 GHz, the finding of Leslie et al. (2017) could be in line with a more extended tail in radio than $H\alpha$ in SOS 114372 (and to a lesser extent in SOS 90630). Following their work, an older stellar population could be more easily detected and more extended in the radio because it takes time for the radio emission to be produced in supernovae and for the cosmic rays to be transported far away from the galaxy disc along the tails. The galaxy was also observed with MUSE by Poggianti et al. (2019). They observed a ionised gas tail consistent with the radio tail length at 1283 MHz, but still much shorter than the radio tail observed at 943 MHz.

Also for this galaxy, we tentatively estimate the velocity of the stripped plasma. The radiative age (~ 90 Myr) in tail2 can be associated to a tail length of 38 kpc (see Fig. 2). After correction for the projection effects, i.e. accounting for an angle $\phi \sim 54$ deg between the wind velocity and the line of sight provided by the simulations, we obtain a velocity of stripped non-thermal component of $\sim 510 \text{ km s}^{-1}$ which is $2.7\times$ lower than the wind velocity ($V_{ICM} = 1400 \text{ km s}^{-1}$) inferred from the N -body/hydrodynamical simulations of RPS run for SOS 114372. However, we notice that the simulations ran by Merluzzi et al. (2013) did not include galactic magnetic fields. If the ram pressure differently affects the gas and the non-thermal component in the galaxy, it is also possible that the radio continuum and the ionised gas tails present different morphology which cannot be foreseen by the simulations now available for SOS 114372.

5.3 The environment of the RPS galaxies

5.3.1 SOS 90630 in the poor cluster SC 1327-312

The cluster SC 1327-312 has a well defined centre with the peak of the X-ray emission coinciding with a bright galaxy. The velocity dispersion of the cluster is $535 \pm 17 \text{ km s}^{-1}$ (Haines et al. 2018). The cluster lies almost entirely within the virial radius of A 3558 and it remains hard to disentangle the two clusters. In particular, SOS 90630 is located in the outskirts of SC 1327-312, $0.2r_{200}$ SW with respect to the centre.

Bardelli et al. (2002) analysed the X-ray gas profile of SC 1327-312 showing that it is rather symmetric. However, the whole SSC shows a continuous filamentary structure 2 degrees in extent, that is filled with hot gas as seen by both Planck and *XMM-Newton* satellite (Planck Collaboration et al. 2014; Merluzzi et al. 2013). Haines et al. (2006) identified two clear overdensities of blue supercluster galaxies in the western region of the poor cluster SC 1329-313, and a linear structure bisecting the clusters A 3558 and SC 1327-312. This is actually the region where the clusters A3562 and A3558 are both experiencing merging events, which may suggest that this merging has recently triggered star formation in these blue galaxies, possibly through shock fronts produced when the ICMs of merging clusters collide. Alternatively, these overdensities could reflect infall regions along the filament connecting the clusters A3558 and A3562. All this places SOS 90630 in an environment where cluster interactions occurred and/or are ongoing.

The role of the magnetic field in RPS events has been investigated by Tonnesen & Stone (2014) who ran magnetohydrodynamical simulations of RPS including a galactic magnetic field. Their work showed that the total amount of gas stripped in the magnetised galaxies does not significantly differ from that removed in unmagnetised ones. They do not find any dramatic difference in the morphology of the tails with and without magnetic field, although the magnetic fields in the disc lead to larger unmixed structures in the tail. Actually, we observe a fragmented ionised gas tail in SOS 90630.

Ruszkowski et al. (2014) simulated the interaction of disc galaxies orbiting in a cluster and exposed to a uniformly magnetised wind including radiative cooling and self-gravity of the gas. Such an interaction produces a very filamentary structure in the tails which then appear bifurcated in the plane of the sky. These features could be distinguished in the tail of SOS 90630 suggesting that the galaxy is exposed to a uniformly magnetised wind.

We should mention that if the RPS explains the truncation of the gas disc as well as other features (gas distribution and star formation in the galaxy disc), the length of the ionised gas tail needs the help of another force to be reproduced. Merluzzi et al. (2016) suggested that both RPS and the tidal interaction with a massive companion whose external edge is visible in the lower right corner of Fig. 3) contribute to the formation of the long tail, as observed in other galaxies (e.g. Gavazzi et al. 2001; Vollmer et al. 2005). We notice that the simulations of Merluzzi et al. (2016) assumed that a constant ram pressure is exerted on the galaxy disc. On the other hand, Tonnesen (2019) showed that varying the ram pressure strength along the galaxy orbit leads to significantly different density and velocity structure in the tail. This new evidence given by the simulations implies that we cannot exclude *a priori* that SOS 90630 is actually affected by RPS alone.

5.3.2 SOS 114372 in the rich cluster A 3558

The bright and massive ($M_{\star} = 7.7 \times 10^{11} M_{\odot}$) galaxy SOS 114372 is a member of the rich cluster A 3558 having a velocity dispersion

of $1007 \pm 25 \text{ km s}^{-1}$ (Haines et al. 2018). The galaxy is located $\sim 1 \text{ Mpc}$ from the cluster centre which corresponds to $0.4r_{200}$, in an environment characterised by a lower density with respect to the very cluster core. SOS 114372 demonstrates that RPS can affect bright ($L > L^{\star}$) and massive cluster galaxies both within and beyond the cluster core (e.g. Crowl & Kenney 2006, 2008; Chung et al. 2007) and thus showing that the ICM is neither static nor homogeneous.

Actually, a non-homogeneous ICM is expected for non-virialized merging and post-merging clusters as those in the SSC. From the analysis of *XMM-Newton* and *Chandra* observations, Rossetti et al. (2007) identified a cold front in the A 3558 ICM probably caused by the sloshing of the core induced by the perturbation of the gravitational potential associated with a past merger. This cold front is expanding, perturbing the density and the temperature of the ICM. From their Fig. 3 it is clear that the cold front is moving in the direction of SOS 114372 and that it is $\sim 5 \text{ arcmin}$ ($\approx 300 \text{ kpc}$ in projection) from the galaxy. Unfortunately, the X-ray observations do not include the region of SOS 114372.

5.3.3 ShaSS 421: a massive galaxy member of AS 0726

ShaSS 421 is a peculiar case of a massive galaxy affected by RPS in a low-density environment. In fact, the parent clusters of ShaSS 421, AS 0726, presents an extremely low X-ray luminosity $L_{X,bol} = 6.9 \times 10^{42} \text{ erg s}^{-1}$ and gas temperature $T_X = 0.90 \text{ keV}$ (ROSAT detection, De Filippis et al. 2005). On the other hand, thanks to the newly acquired redshifts in this area, Haines et al. (2018) measured a velocity dispersion of $603 \pm 48 \text{ km s}^{-1}$ and the corresponding dynamical mass of $M_{200} = 2.4 \times 10^{14} M_{\odot}$, which suggests a hotter and denser ICM with respect to the ROSAT detection. Beside this, the dynamical analysis revealed that AS 0726 is a system of 2-3 groups with ShaSS 421 associated to the most prominent peak in the galaxy spatial distribution. Therefore, the complex and unrelaxed dynamics of AS 0726 could contribute to the ongoing RPS observed in ShaSS 421. The group-group merger would either trigger a shock front in the ICM, or allow the high encounter velocity between ICM and galaxy (see Owers et al. 2012b; Venturi et al. 2022).

A detailed analysis of this galaxy is ongoing by means of deep MUSE data.

5.3.4 SOS 61086 in the poor cluster SC 1329-313

SOS 61086 is a member of the poor cluster SC 1329-313. The galaxy shows both $H\alpha$ and radio tails extending out to 30 kpc north of the disc. The tail orientation, as projected in the sky, is almost tangential to the cluster outskirts suggesting that the galaxy orbit is not radial.

Venturi et al. (2022) detected an inter-cluster radio bridge at GHz frequencies which extends between the cluster A 3562 and the group SC 1329-313. This bridge takes the form of an arc which connects the cluster and the group from north, and remarkably follows the X-ray emission in this region. The authors interpreted the observed low brightness intercluster diffuse radio emission as a trace of turbulence injected in the ICM by the flyby of SC 1329-313 north of A 3562 into the supercluster core (see Finoguenov et al. 2004). Because of its position, the trajectory of SC 1329-313 falling into the SSC, and the tail orientation, SOS 61086 is the textbook case of a galaxy where the RPS is triggered by the perturbed ICM during a minor merger event.

6 SUMMARY AND CONCLUSIONS

In this work we study a sample of four galaxies undergoing ram-pressure stripping in different environments of the Shapley supercluster. The radio continuum emission of three of them (SOS 90630, SOS 114372 and ShaSS 421) is analysed here for the first time. Radio observations collected with various interferometers and spanning the frequency range from 235 to 1367 MHz are available for the galaxies SOS 90630, SOS 114372 and SOS 61086, while only 887 MHz ASKAP observations cover ShaSS 421.

SOS 90630 and SOS 114372 both show radio continuum extraplanar emission in different radio bands. At 1.283 GHz MeerKAT radio continuum tails extend ~ 40 kpc in projection out of the disc, while we do not detect a radio continuum tail in the ASKAP data of ShaSS 421.

Together with the total flux, in the tailed galaxies we are able to disentangle the radio emission of the galaxy and the inner tail (gal+tail1) from that of the outer tail (tail2). By means of the multi-frequency dataset, we derive the spectral index along the tails, which in both galaxies steepens in the outer tail as it was also observed in the fourth galaxy (SOS 61086, [Venturi et al. 2022](#)). Furthermore, we derive the inband spectral index across the disc of SOS 114372 and the disc and inner tail of SOS 90630 from the 1.28 GHz MeerKAT data. In both galaxies the tail of relativistic electrons is superimposed to the tail of ionised gas as traced by H α emission. However, at 1.28 GHz the radio tail extends in projection with almost the same length of the optical tail for SOS 90630 (as for SOS 61086), while for SOS 114372 the length of radio tail significantly exceeds that of the optical one.

We interpret our findings in the framework of the RPS scenario, which was ascertained for these galaxies by the analysis of IFS observations, multi-band data and N -body/hydrodynamical simulations ([Merluzzi et al. 2013, 2016](#)).

In SOS 90630 and SOS 114372 the consistency among *i*) the epoch of the onset of stripping (inferred by the hydrodynamical simulations); *ii*) the age of the youngest stellar population (derived by the IFS data) and *iii*) the radiative age of the electrons in the tail (obtained from the synchrotron spectrum) supports a scenario where the radio emitting plasma and the warm gas tails are related to the same event, i.e. by the ram pressure, with similar efficiency. This was also the case of SOS 61086 ([Venturi et al. 2022](#)).

SOS 90630. Taking into account the steepening of the spectral index, the ageing of the electrons and the source (HII regions) of the gas excitation in the tail, we suggest that the radio emission of the inner tail is due to electrons stripped from the galaxy disc, while in the outer tail we cannot exclude a contribution due to *in situ* star formation, which would account for the modest ageing observed in this region.

SOS 114372. The steepening of the spectral index indicates that also in this galaxy the relativistic electrons origin from the disc, however the H α emission in the tail is mainly powered by shock excitation which may accelerate also the relativistic electrons and explain their modest ageing in the outer tail.

Considering also SOS 61086, the three detected radio tails are all fuelled by relativistic electrons stripped with the plasma from the disc. However, while the electrons in the tail of SOS 61086 do not show any signs of re-acceleration or rejuvenation, those in the tails of the other two galaxies are likely either accelerated by shock excitation (SOS 114372) or further powered by *in situ* star formation (SOS 90630).

It is remarkable that all the galaxies of our sample are located in environments where cluster-cluster interaction occurred and/or is

ongoing. We underline again that the galaxies considered in this work are the most dramatically affected by RPS across the ShaSS region.

The correlation between clusters and groups merger and RPS events has been suggested by [Owers et al. \(2012a\)](#) who identified three RPS galaxies showing active star formation in their tails in Abell 2744. Being these objects found in close proximity to the merger-related feature, the authors proposed that the observed star formation has been triggered by the rapid increase in pressure during an interaction with the shock front. [McPartland et al. \(2016b\)](#) conducted a systematic search for RPS galaxies in 63 MACS clusters at intermediate redshifts identifying 53 RPS candidates. Their analysis of a three-dimensional modelling of the orbits of the galaxies suggests that the most extreme events are primarily triggered in massive cluster mergers where the RPS may initiate far from the cluster core because of the large relative (galaxies-ICM) velocities. This could be actually the case of SOS 114372. In addition, [McPartland et al. \(2016b\)](#) suggested that extreme RPS can also occur in mergers of poor clusters and groups. This is likely what we observe for ShaSS 421 in the unrelaxed poor cluster AS 0726.

A first theoretical study of RPS in the environment of galaxy cluster merges was presented by [Ruggiero et al. \(2019\)](#) considering the A901/2 system where two clusters and two groups are simultaneously merging. They concluded that the galaxies experiencing RPS are preferentially located near a boundary where the gas moving with the cluster/subcluster and the gas from the remaining of the system collide. This recalls the case of SOS 61086 affected by RPS along the trajectory of the poor cluster SC 1329-313 falling into the SSC.

If cluster-cluster interaction plays a role in favouring the RPS, as it seems, then the detection of RPS events can be used as a diagnostic tool to constrain the geometry of cluster collision as proposed by [Ebeling & Kalita \(2019\)](#). Actually, the orientation of the tail of SOS 61086 supports and reinforces the scenario of the minor merger of SC 1329-313 and A 3562 in the SSC, as recently traced by the intercluster diffuse emission detected at 1.28 GHz by MeerKAT (see [Venturi et al. 2022](#)).

The question now is why our sample is limited to four galaxies experiencing RPS across the harsh environment of the Shapley supercluster. These ascertained cases of ongoing RPS have been selected from the optical images, thus biased to objects showing star formation and/or shock excitation of the gas into the tail. Different biases, both observational and intrinsic to the mechanism (e.g. the short duration of the stripping event), make it difficult to identify RPS candidates and deep/telescope time expensive IFS observations are needed to trace low brightness extraplanar ionised gas. Therefore, even if the information provided by IFS observations will be always essential, the current available and forthcoming radio facilities (MeerKAT, LOFAR, uGMRT, ASKAP) will allow to map the atomic gas content and detect extra-planar atomic hydrogen as well as to detect tails of non thermal component by means of blind surveys of large sky regions (e.g. [Roberts et al. 2021a](#)). We aim to use this approach to make a census of RPS galaxies and possibly trace their radio continuum and HI tails in the Shapley supercluster.

7 ACKNOWLEDGEMENTS

The authors thank the referee for helping them to improve their work. PM, TV, VC and GB acknowledge INAF Mini Grant 2022 *ShaSEE - Shapley Supercluster Exploration and Exploitation*. Basic research in radio astronomy at the Naval Research Laboratory is supported by 6.1 Base funding. This work was supported in part by the Italian Ministry of Foreign Affairs and International Cooper-

ation, grant number ZA23GR03. We thank the staff of the GMRT that made these observations possible. GMRT is run by the National Centre for Radio Astrophysics of the Tata Institute of Fundamental Research. This scientific work uses data obtained from Inyarrimanha Ilgari Bundara / the Murchison Radio-astronomy Observatory. We acknowledge the Wajarri Yamaji People as the Traditional Owners and native title holders of the Observatory site. CSIRO ASKAP radio telescope is part of the Australia Telescope National Facility (<https://ror.org/05qajvd42>). Operation of ASKAP is funded by the Australian Government with support from the National Collaborative Research Infrastructure Strategy. ASKAP uses the resources of the Pawsey Supercomputing Research Centre. Establishment of ASKAP, Inyarrimanha Ilgari Bundara, the CSIRO Murchison Radio-astronomy Observatory and the Pawsey Supercomputing Research Centre are initiatives of the Australian Government, with support from the Government of Western Australia and the Science and Industry Endowment Fund. The MeerKAT telescope is operated by the South African Radio Astronomy Observatory, which is a facility of the National Research Foundation, an agency of the Department of Science and Innovation. Based on observations collected at the European Organisation for Astronomical Research in the Southern Hemisphere under ESO programmes 097.B-0917(A) and 099.B-0016(A).

DATA AVAILABILITY

In this work we exploit the radio continuum observations of the Australian Square Kilometre Array Pathfinder (ASKAP, [Hotan et al. 2021](#)). In particular, at 887 MHz we used the data of the survey EMU Evolutionary Map of the Universe ([Norris et al. 2011](#), <http://emu-survey.org/>) together with the Early Science Project ESP 20 ([Venturi et al. 2022](#)), and at 943 MHz and 1367 MHz the data of the POSSUM (Polarization Sky Survey of the Universe's Magnetism, [Gaensler et al. 2010](#), <https://possum-survey.org/science/>) Pilot2 survey. We also benefit of one pointing of the MeerKAT Galaxy Cluster Legacy Survey (MGCLS, [Knowles et al. 2022](#)) at 1283 MHz. The VST *r*-band images of the galaxies have been collected and analysed in the Shapley Supercluster Survey (ShaSS, [Merluzzi et al. 2015](#)). The raw images are available through the ESO archive (<http://archive.eso.org/cms.html>), ESO Programmes 096.A-0129 091.A-0050, 089.A-0095, 090.B-0414. The reduced *r*-band images can be provided by the authors upon request. The ESO MUSE observations of ShaSS 421 (ESO Programme 097.B-0917) will be published by Merluzzi et al. (in preparation).

REFERENCES

- Abramson A., Kenney J. D. P., 2014, *AJ*, **147**, 63
- Bacon R., et al., 2010, in McLean I. S., Ramsay S. K., Takami H., eds, Society of Photo-Optical Instrumentation Engineers (SPIE) Conference Series Vol. 7735, Ground-based and Airborne Instrumentation for Astronomy III. p. 773508, [doi:10.1117/12.856027](https://doi.org/10.1117/12.856027)
- Balkowski C., Vollmer B., Cayatte V., 2001, *ApSS*, **277**, 393
- Balogh M. L., Navarro J. F., Morris S. L., 2000, *ApJ*, **540**, 113
- Bamford S. P., Nichol R. C., Baldry I. K., Land K., Lintott C. J., et al. 2009, *MNRAS*, **393**, 1324
- Bardelli S., Pisani A., Ramella M., Zucca E., Zamorani G., 1998, *MNRAS*, **300**, 589
- Bardelli S., De Grandi S., Ettori S., Molendi S., Zucca E., Colafrancesco S., 2002, *A&A*, **382**, 17
- Bekki K., 2009, *MNRAS*, **399**, 2221
- Bellhouse C., et al., 2019, *MNRAS*, **485**, 1157
- Bellhouse C., et al., 2021, *MNRAS*, **500**, 1285
- Boselli A., Gavazzi G., 2006, *PASP*, **118**, 517
- Boselli A., Cortese L., Boquien M., Boissier S., Catinella B., Gavazzi G., Lagos C., Saintonge A., 2014, *A&A*, **564**, A67
- Boselli A., et al., 2018, *A&A*, **614**, A56
- Boselli A., Fossati M., Sun M., 2022, *A&ARv*, **30**, 3
- Brown T., et al., 2017, *MNRAS*, **466**, 1275
- Brown T., et al., 2021, *ApJS*, **257**, 21
- Camilo F., et al., 2018, *ApJ*, **856**, 180
- Casasola V., Bettoni D., Galletta G., 2004, *A&A*, **422**, 941
- Chen H., et al., 2020, *MNRAS*, **496**, 4654
- Chung A., van Gorkom J. H., Kenney J. D. P., Vollmer B., 2007, *ApJL*, **659**, L115
- Chyży K. T., Soida M., Bomans D. J., Vollmer B., Balkowski C., Beck R., Urbanik M., 2006, *A&A*, **447**, 465
- Condon J. J., Cotton W. D., Greisen E. W., Yin Q. F., Perley R. A., Taylor G. B., Broderick J. J., 1998, *AJ*, **115**, 1693
- Consolandi G., Gavazzi G., Fossati M., Fumagalli M., Boselli A., Yagi M., Yoshida M., 2017, *A&A*, **606**, A83
- Corbelli E., et al., 2012, *A&A*, **542**, A32
- Cowie L. L., Songalia A., 1977, *Nature*, **266**, 501
- Crowl H. H., Kenney J. D. P., 2006, *ApJL*, **649**, L75
- Crowl H. H., Kenney J. D. P., 2008, *AJ*, **136**, 1623
- Davies J. I., et al., 2019, *A&A*, **626**, A63
- De Filippis E., Schindler S., Erben T., 2005, *A&A*, **444**, 387
- Dopita M., Hart J., McGregor P., Oates P., Bloxham G., Jones D., 2007, *ApSS*, **310**, 255
- Dopita M., et al., 2010, *ApSS*, **327**, 245
- Duchesne S. W., et al., 2023, *arXiv e-prints*, p. [arXiv:2306.07194](https://arxiv.org/abs/2306.07194)
- Ebeling H., Kalita B. S., 2019, *ApJ*, **882**, 127
- Ebeling H., Stephenson L. N., Edge A. C., 2014, *ApJ*, **781**, L40
- Ettori S., Fabian A. C., White A. A., 1997, *MNRAS*, **289**, 787
- Feretti L., Giovannini G., Klein U., Mack K. H., Sijbring L. G., Zech G., 1998, *A&A*, **331**, 475
- Finoguenov A., Henriksen M. J., Briel U. G., de Plaa J., Kaastra J. S., 2004, *ApJ*, **611**, 811
- Fossati M., Fumagalli M., Boselli A., Gavazzi G., Sun M., Wilman D. J., 2016, *MNRAS*, **455**, 2028
- Fossati M., Fumagalli M., Gavazzi G., Consolandi G., Boselli A., Yagi M., Sun M., Wilman D. J., 2019, *MNRAS*, **484**, 2212
- Fumagalli M., Fossati M., Hau G. K. T., Gavazzi G., Bower R., Sun M., Boselli A., 2014, *MNRAS*, **445**, 4335
- Gaensler B. M., Landecker T. L., Taylor A. R., POSSUM Collaboration 2010, in American Astronomical Society Meeting Abstracts #215. p. 470.13
- Gavazzi G., 1978, *A&A*, **69**, 355
- Gavazzi G., Contursi A., Carrasco L., Boselli A., Kennicutt R., Scodreggio M., Jaffe W., 1995, *A&A*, **304**, 325
- Gavazzi G., Boselli A., Mayer L., Iglesias-Paramo J., Vilchez J. M., Carrasco L., 2001, *ApJ*, **563**, L23
- Giacintucci S., et al., 2005, *A&A*, **440**, 867
- Giacintucci S., et al., 2022, *ApJ*, **934**, 49
- Govoni F., Feretti L., 2004, *International Journal of Modern Physics D*, **13**, 1549
- Guiderdoni B., Rocca-Volmerange B., 1985, *A&A*, **151**, 108
- Gunn J. E., Gott J. R. I., 1972, *ApJ*, **176**, 1
- Gupta Y., et al., 2017, *Current Science*, **113**, 707
- Haines C. P., Merluzzi P., Mercurio A., Gargiulo A., Krusanova N., Busarello G., La Barbera F., Capaccioli M., 2006, *MNRAS*, **371**, 55
- Haines C. P., Busarello G., Merluzzi P., Smith R. J., Raychaudhury S., Mercurio A., Smith G. P., 2011, *MNRAS*, **412**, 127
- Haines C. P., et al., 2018, *MNRAS*, **481**, 1055
- Hernquist L., 1990, *ApJ*, **356**, 359
- Higuchi Y., Okabe N., Merluzzi P., Haines C. P., Busarello G., Grado A., Mercurio A., 2020, *MNRAS*, **497**, 52
- Hotan A. W., et al., 2021, *PASA*, **38**, 9
- Intema H. T., van der Tol S., Cotton W. D., Cohen A. S., van Bemmell I. M., Röttgering H. J. A., 2009, *A&A*, **501**, 1185
- Jáchym P., Köppen J., Palouš J., Combes F., 2009, *A&A*, **500**, 693
- Jaffe W. J., Perola G. C., 1973, *A&A*, **26**, 423

- Johnston S., et al., 2008, *Exp. Astr.*, **22**, 151
- Knowles K., et al., 2022, *A&A*, **657**, A56
- Lal D. V., et al., 2022, *ApJ*, **934**, 170
- Larson R. B., Tinsley B. M., Caldwell C. M., 1980, *ApJ*, **237**, 692
- Leslie S. K., et al., 2017, *MNRAS*, **471**, 2438
- Marcolini A., Brighenti F., D’Ercole A., 2003, *MNRAS*, **345**, 1329
- McPartland C., Ebeling H., Roediger E., Blumenthal K., 2016a, *MNRAS*, **455**, 2994
- McPartland C., Ebeling H., Roediger E., Blumenthal K., 2016b, *MNRAS*, **455**, 2994
- Mercurio A., et al., 2015, *MNRAS*, **453**, 3685
- Merluzzi P., et al., 2013, *MNRAS*, **429**, 1747
- Merluzzi P., et al., 2015, *MNRAS*, **446**, 803
- Merluzzi P., Busarello G., Dopita M. A., Haines C. P., Steinhauser D., Bourdin H., Mazzotta P., 2016, *MNRAS*, **460**, 3345
- Merluzzi P., Busarello G., Dopita M. A., Thomas A. D., Haines C. P., Grado A., Limatola L., Mercurio A., 2018, *ApJ*, **852**, 113
- Miller N. A., 2005, *AJ*, **130**, 2541
- Miller N. A., Hornschemeier A. E., Mobasher B., 2009, *AJ*, **137**, 4436
- Mo H. J., Mao S., White S. D. M., 1998, *MNRAS*, **295**, 319
- Murgia M., Fanti C., Fanti R., Gregorini L., Klein U., Mack K. H., Vigotti M., 1999, *A&A*, **345**, 769
- Murphy E. J., Kenney J. D. P., Helou G., Chung A., Howell J. H., 2009, *ApJ*, **694**, 1435
- Norris R. P., et al., 2011, *PASA*, **28**, 215
- Owers M. S., Couch W. J., Nulsen P. E. J., Randall S. W., 2012a, *ApJ*, **750**, L23
- Owers M. S., Couch W. J., Nulsen P. E. J., Randall S. W., 2012b, *ApJL*, **750**, L23
- Planck Collaboration et al., 2013, arXiv:1303.5089,
- Planck Collaboration et al., 2014, *A&A*, **571**, A29
- Poggianti B. M., et al., 2016, *AJ*, **151**, 78
- Poggianti B. M., et al., 2017, *ApJ*, **844**, 48
- Poggianti B. M., et al., 2019, *MNRAS*, **482**, 4466
- Proust D., et al., 2006, *A&A*, **447**, 133
- Quintana H., Proust D., Dünner R., Carrasco E. R., Reisenegger A., 2020, *A&A*, **638**, A27
- Raychaudhury S., 1989, *Nature*, **342**, 251
- Roberts I. D., et al., 2021a, *A&A*, **650**, A111
- Roberts I. D., van Weeren R. J., McGee S. L., Botteon A., Ignesti A., Rottgering H. J. A., 2021b, *A&A*, **652**, A153
- Roberts I. D., et al., 2023, arXiv e-prints, p. arXiv:2310.20417
- Roediger E., Brüggén M., 2006, *MNRAS*, **369**, 567
- Roediger E., Hensler G., 2005, *A&A*, **433**, 875
- Rossetti M., Ghizzardi S., Molendi S., Finoguenov A., 2007, *A&A*, **463**, 839
- Ruggiero R., Machado R. E. G., Roman-Oliveira F. V., Chies-Santos A. L., Lima Neto G. B., Doubrawa L., Rodríguez del Pino B., 2019, *MNRAS*, **484**, 906
- Ruszkowski M., Brüggén M., Lee D., Shin M. S., 2014, *ApJ*, **784**, 75
- Sanderson A. J. R., Ponman T. J., 2010, *MNRAS*, **402**, 65
- Shapley H., 1930, *Harvard College Observatory Bulletin*, **874**, 9
- Springel V., 2005, *MNRAS*, **364**, 1105
- Springel V., 2010, *MNRAS*, **401**, 791
- Springel V., Di Matteo T., Hernquist L., 2005, *MNRAS*, **361**, 776
- Swarup G., Ananthakrishnan S., Kapahi V. K., Rao A. P., Subrahmanya C. R., Kulkarni V. K., 1991, *Current Science*, **60**, 95
- Tabatabaei F. S., et al., 2017, *ApJ*, **836**, 185
- Tonnesen S., 2019, *ApJ*, **874**, 161
- Tonnesen S., Stone J., 2014, *ApJ*, **795**, 148
- Venturi T., Bardelli S., Morganti R., Hunstead R. W., 2000, *MNRAS*, **314**, 594
- Venturi T., Bardelli S., Dallacasa D., Brunetti G., Giacintucci S., Hunstead R. W., Morganti R., 2003, *A&A*, **402**, 913
- Venturi T., et al., 2022, *A&A*, **660**, A81
- Vollmer B., Cayatte V., Balkowski C., Duschl W. J., 2001, *ApJ*, **561**, 708
- Vollmer B., Beck R., Kenney J. D. P., van Gorkom J. H., 2004a, *AJ*, **127**, 3375
- Vollmer B., Balkowski C., Cayatte V., van Driel W., Huchtmeier W., 2004b, *A&A*, **419**, 35
- Vollmer B., Huchtmeier W., van Driel W., 2005, *A&A*, **439**, 921
- Vollmer B., Soida M., Chung A., Chemin L., Braine J., Boselli A., Beck R., 2009, *A&A*, **496**, 669
- Vollmer B., Soida M., Chung A., Beck R., Urbanik M., Chyży K. T., Otmianowska-Mazur K., van Gorkom J. H., 2010, *A&A*, **512**, A36
- Vollmer B., Soida M., Beck R., Chung A., Urbanik M., Chyży K. T., Otmianowska-Mazur K., Kenney J. D. P., 2013, *A&A*, **553**, A116
- Vollmer B., Pappalardo C., Soida M., Lançon A., 2018, *A&A*, **620**, A108
- Vulcani B., et al., 2021, *ApJ*, **914**, 27
- Westcott J., Brinks E., Hindson L., Beswick R., Heesen V., 2018, *MNRAS*, **475**, 5116

APPENDIX A: FULL RESOLUTION AND CONVOLVED RADIO IMAGES OF THE GALAXIES SOS 90630 AND SOS 114372

In this section we show the radio images of the two galaxies newly studied in this work and for which multi-frequency radio observations are available (see Table 2 for the angular resolution and rms of each image). The full resolution images are shown in Figs. A1 and A2, while the images convolved to 18×18 arcsec² are shown in Figs. A3 and A4.

APPENDIX B: SPECTRAL FITS

In Table 3 we give the fluxes measured from the radio images convolved to the resolution of 18×18 arcsec² except GMRT 235 MHz for SOS 90630. In Fig. B1 we plot the spectral fits to the data in Table 3 for SOS 90630 and SOS 114372 obtained with the program Synage (Murgia et al. 1999). The parameters used for the fit are detailed in Sections 4.1 and 4.2.

APPENDIX C: N-BODY/HYDRODYNAMICAL SIMULATIONS OF THE RPS GALAXIES

The main goal of the simulations is to understand to what extent ram pressure might explain the main observed features of the gas: the truncation of the disc, the shape and extension of the tail and the kinematics. We ran N-body/hydrodynamical simulations for the galaxies SOS 114372, SOS 90630 and SOS 61086 in Merluzzi et al. (2013, 2016) to which we refer for a complete description. The aim of the simulations was to reproduce as closely as possible the observed velocity field of the gas and thus constrain the ICM wind angle and velocity and the time of the onset of ram pressure. The simulations were run from wind angles close to edge-on to close to face-on at intervals of 10° and the wind velocity range was set taking into account as the lower limit the galaxy line-of-sight velocity relative to the cluster systemic velocity and as the upper limit the escape velocity (derived from the Hernquist model of each cluster). The ICM densities were derived from the X-ray profile of each cluster (Sanderson & Ponman 2010; Merluzzi et al. 2016).

For the three galaxies the simulations were performed adopting a model galaxy resembling the pre-interaction properties of each galaxy. The initial conditions are calculated according to Springel et al. (2005) based on the work of Mo et al. (1998). Our model galaxy includes a dark matter halo, a stellar disc, a gaseous disc and a stellar bulge. The disc scale length of the galaxy is directly related to the angular momentum of the disc with the spin as a free parameter. The stellar and gaseous disc have exponential surface density profiles. For the stellar bulge and the dark matter halo a Hernquist (1990) profile is adopted.

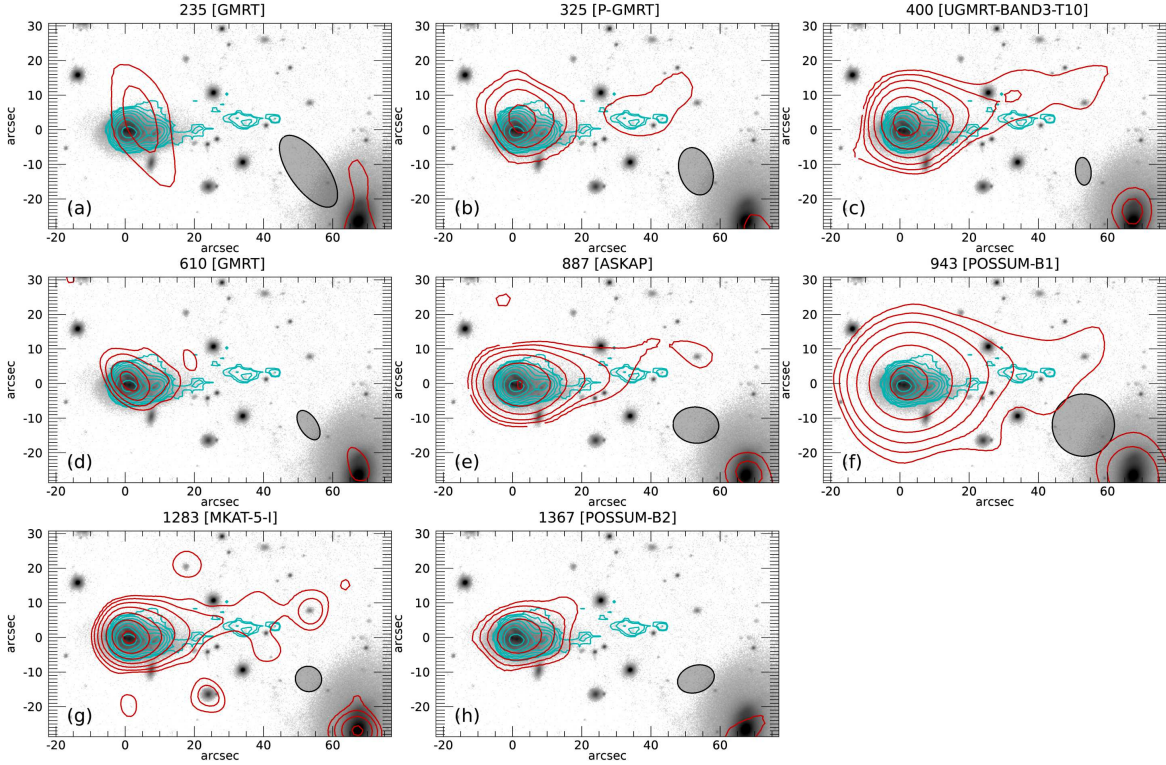


Figure A1. Full resolution radio images (red contours) in all the bands for the galaxy SOS 90630 superimposed to the VST r -band image. On top of each panel the frequency (MHz) and instrument are indicated (see Table 2 for details). The contours start from $3\times\text{rms}$ and are spaced by a factor 2 in flux. The cyan contours map the $H\alpha$ emission. The beam is represented by the gray ellipse.

The simulations were done with the cosmological N -body/hydrodynamic code GADGET-2 (Springel 2005) for SOS 114372 while the cosmological moving-mesh code AREPO (Springel 2010) is used for SOS 90630 and SOS 61086 (for details see Merluzzi et al. 2013, 2016).

This paper has been typeset from a $\text{T}_{\text{E}}\text{X}/\text{L}^{\text{A}}\text{T}_{\text{E}}\text{X}$ file prepared by the author.

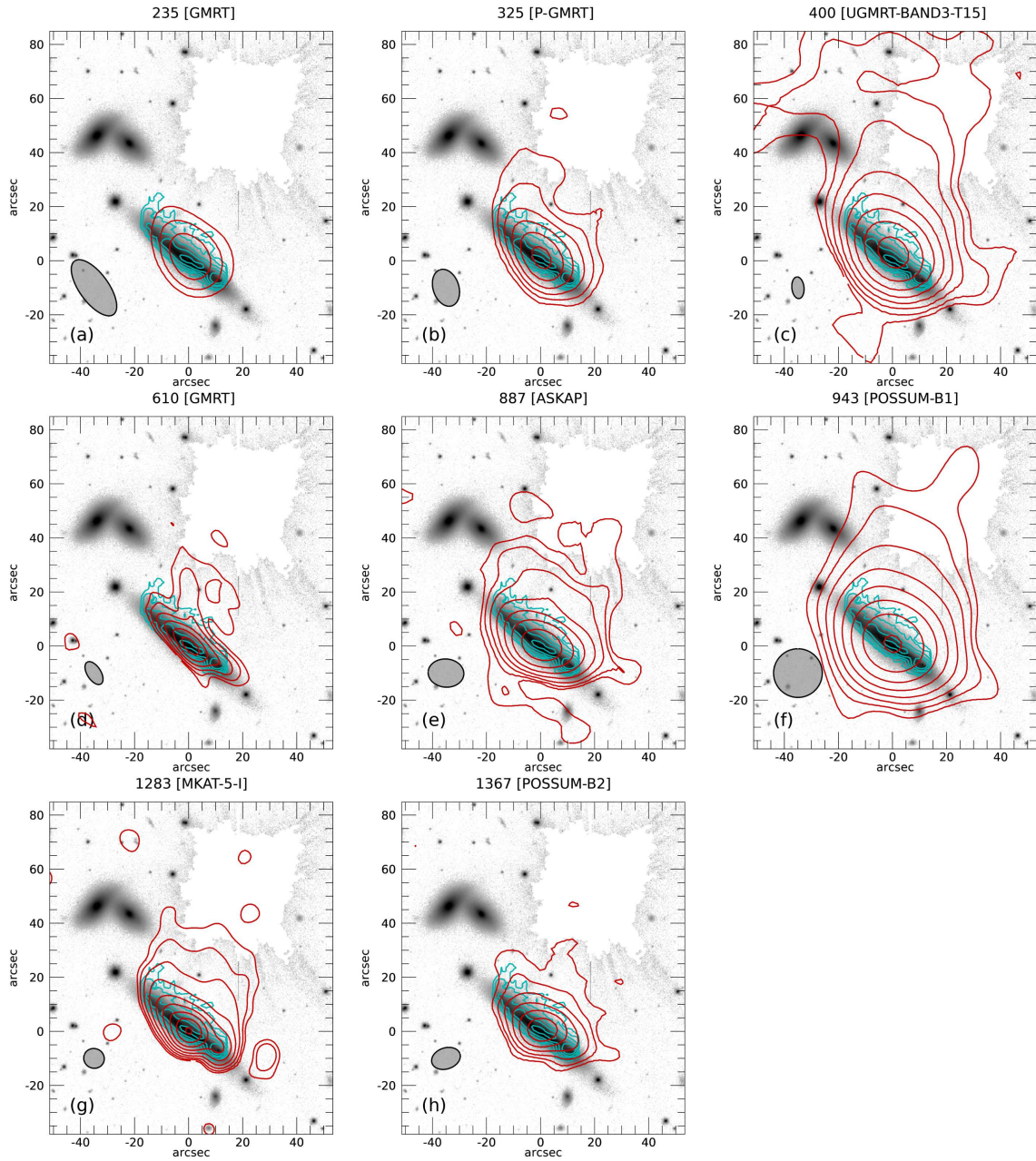


Figure A2. Same of Fig. A1 for SOS 114372.

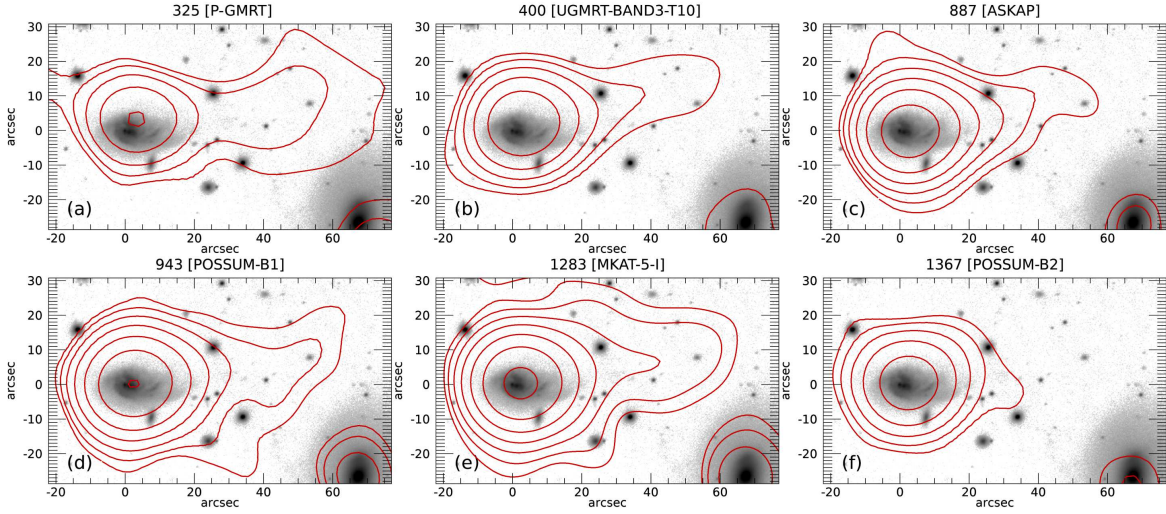


Figure A3. Radio contours (red) convolved to $18 \times 18 \text{ arcsec}^2$ in all the bands for the galaxy SOS 90630 superimposed to the VST r -band image. On top of each panel the frequency (MHz) and instrument are indicated (see Table 2 for details). The contours start from $3 \times \text{rms}$ and are spaced by a factor 2 in flux.

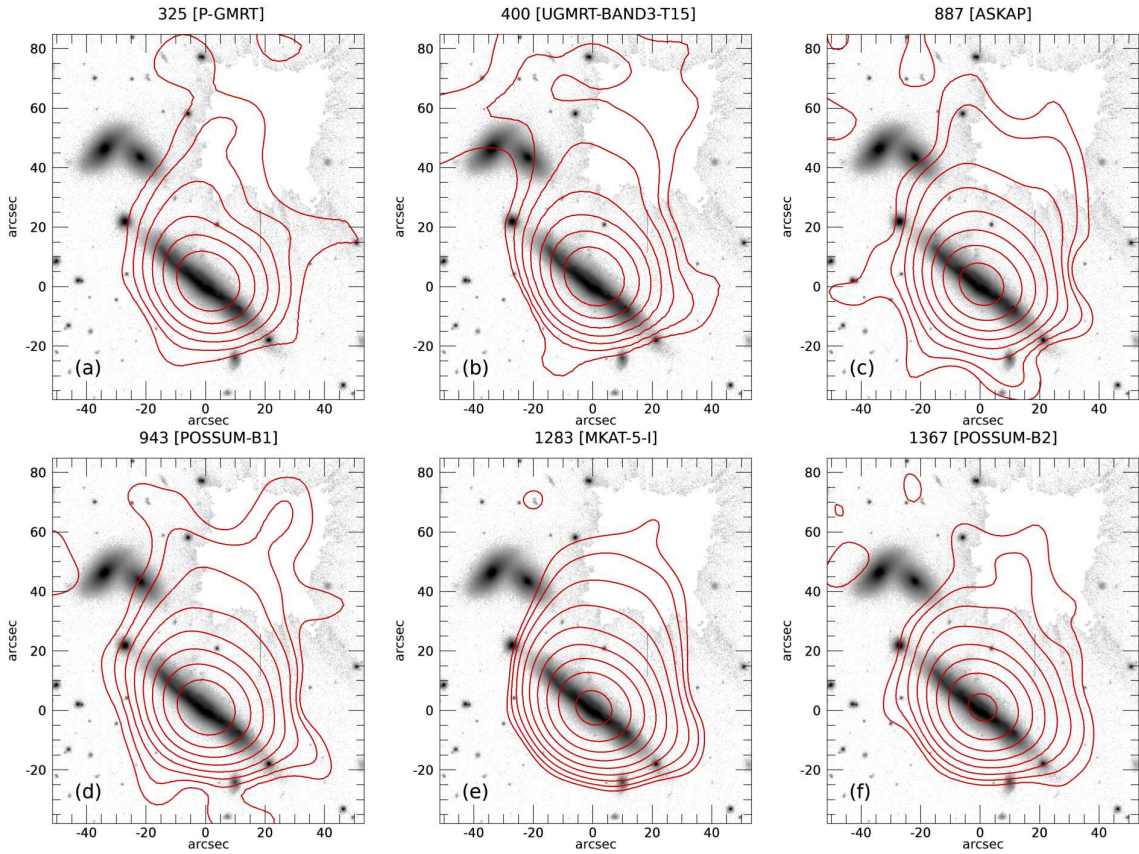


Figure A4. Same of Fig. A3 for SOS 114372.

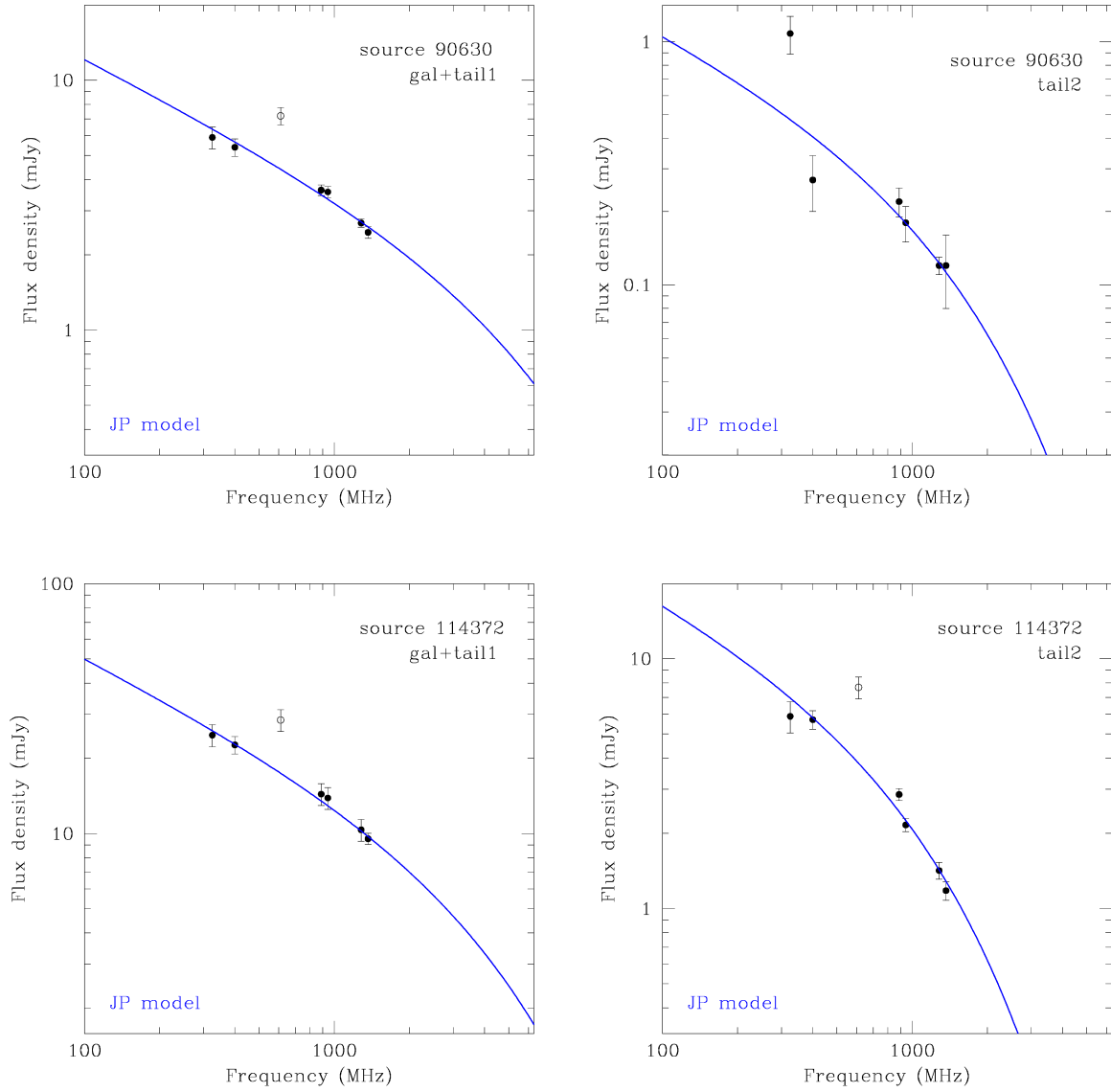


Figure B1. Spectral fits obtained for the component gal+tail1 and tail2 using the information provided in Table 3 for SOS 90630 (top row) and for SOS 114372 (bottom row). The fluxes at 610 MHz (open circle) were not considered in the fits.